The Removal of Sulfamonomethoxine (SMM) with Copper Oxide/Zirconium Dioxide (CuO/ZrO₂) Nanocomposites by Photocatalytic Degradation in Pharmaceutical Industry Wastewaters and the Evaluation of Microtox (*Aliivibrio fischeri*) and *Daphnia magna* Acute Toxicity Assays

Rukiye Öztekin [a] and Delia Teresa Sponza [a*]

[a] *Department of Environmental Engineering, Engineering Faculty, Dokuz Eylül University, Tınaztepe Campus, 35160 Buca/Izmir, Turkey.*

Authors' contributions

This work was carried out in collaboration between both authors. Both authors read and approved the final manuscript.

Original Research Article

_____

Corresponding author: E-mail: delya.sponza@deu.edu.tr;

ABSTRACT

In this study, Copper oxide/zirconium dioxide (CuO/ZrO$_2$) nanocomposites (NCs) as a photocatalys was examined during photocatalytic degradation process (PDP) in the efficient removal of Sulfamonomethoxine (SMM) from pharmaceutical industry wastewater (PI ww) plant, İzmir, Turkey. Different pH values (3.0, 4.0, 7.0, 9.0, 10.0 and 12.0), increasing SMM concentrations (5, 10, 20 and 40 mg/l), increasing CuO/ZrO$_2$ NCs concentrations (100, 200, 400, 800 and 1000 mg/l), different CuO/ZrO$_2$ NCs mass ratios (1/2, 2/3, 3/4, 4/4, 4/3, 3/2, 2/1), increasing recycle times (1., 2., 3., 4., 5., 6. and 7.) was operated during PDP in the efficient removal of SMM in PI ww. The characteristics of the synthesized nanoparticles (NPs) were assessed using XRD, DRS, FESEM, EDX, FTIR, TEM and XPS analyses, respectively. The acute toxicity assays were operated with Microtox (*Aliivibrio fischeri* also called *Vibrio fischeri*) and *Daphnia magna* acute toxicity tests. The photocatalytic degradation mechanisms of CuO/ZrO$_2$ NCs and the reaction kinetics of SMM were evaluated in PI ww during PDP. Cost analysis was evaluated for SMM removal with CuO/ZrO$_2$ NCs by PDP in PI ww. ANOVA statistical analysis was used for all experimental samples. Maximum 99.6% SMM removal was obtained during PDP in PI ww, at 350 W UV-vis light irradiation power, at 147 mW/cm^2 light intensity, after 120 min, at pH=12.0 and at 25°C, respectively. Maximum 99.2% SMM removal was found with PDP in PI ww, at 5 mg/l SMM, at 350 W UV-vis, at 147 mW/cm^2, after 120 min, at pH=12.0 and at 25°C, respectively. Maximum 99.5% SMM removal was measured to 800 mg/l CuO/ZrO$_2$ NCs with PDP in PI ww, at 5 mg/l SMM, at 350 W UV-vis, at 147 mW/cm^2, after 120 min, at pH=12.0 and at 25°C, respectively. Maximum 99.4% SMM removal was measured at 4/3wt CuO/ZrO$_2$ NCs mass ratios, at 5 mg/l SMM, at 800 mg/l CuO/ZrO$_2$ NCs, at 350 W UV-vis, at 147 mW/cm^2, after 120 min, at pH=12.0 and at 25°C, respectively. Maximum 99.5% SMM recovery was measured in PI ww during PDP, after 1. recycle time, at 5 mg/l SMM, at 800 mg/l CuO/ZrO$_2$ NCs, at 4/3wt CuO/ZrO$_2$ NCs mass rartio, at 350 W UV-vis, at 147 mW/cm^2, after 120 min, at pH=12.0 and at 25°C, respectively. 97.31% maximum Microtox acute toxicity removal was found in SMM=20 mg/l after 180 min, and at 60°C. It was observed an inhibition effect of SMM=40 mg/l to Microtox after 180 min, and at 60°C. 93.27% maximum *Daphnia magna* acute toxicity removal was obtained in SMM=20 mg/l after 180 min, and at 60°C, respectively. It was obtained an inhibition effect of SMM=40 mg/l to *Daphnia magna* after 180 min and at 60°C. As a result, the CuO/ZrO$_2$ NCs during PDP in PI ww was stable in harsh environments such as acidic, alkaline, saline and then was still effective process. Finally, the combination of a simple, easy operation preparation process, excellent performance and cost effective, makes this CuO/ZrO$_2$ NCs a promising option during PDP in PI ww treatment.

1. INTRODUCTION

Emerging contaminants (ECs), sometimes known as contaminants of emerging concern (CECs) can refer to a wide variety of artificial or naturally occurring chemicals or materials that are harmful to human health after long-term disclosure. ECs can be classified into several classes, including agricultural contaminants (pesticides and fertilizers), medicines and antidote drugs, industrial and consumer waste products, and personal care and household cleaning products [1,2]. Antibiotics are one of the ECs that have raised concerns in the previous two decades because they have been routinely and widely used in human and animal health care, resulting in widespread antibiotic residues discharged in surface, groundwater and wastewater.

Antibiotics, which are widely utilized in medicine, poultry farming and food processing [3,4], have attracted considerable attention due to their abuse and their harmful effects on human health

and the ecological environment [5,6]. The misuse of antibiotics induces Deoxyribonucleic Acid (DNA) contamination and accelerates the generation of drug-resistant bacteria and super-bacteria [7-9]; thus, some diseases are more difficult to cure [10]. A number of studies have revealed that the level of antibiotics in the soil, air and surface water, and even in potable water, is excessive in many areas [11-13], which will ultimately accumulate in the human body via drinking water and then damage the body's nervous system, kidneys and blood system. Therefore, it is necessary to develop an efficient method to remove antibiotics present in PI ww.

The uncontrolled, ever-growing accumulation of antibiotics and their residues in the environment is an acute modern problem. Their presence in water and soil is a potential hazard to the environment, humans, and other living beings. Many therapeutic agents are not completely metabolized, which leads to the penetration of active drug molecules into the biological environment, the emergence of new contamination sources, the wide spread of bacteria and microorganisms with multidrug resistance [14-16]. Modern PI ww facilities do not allow efficient removal of antibiotic residues from the environment [17,18], which leads to their accumulation in ecological systems [19,20]. Global studies of river pollution with antibiotics have shown that 65% of surveyed rivers in 72 countries on 6 continents are contaminated with antibiotics [21]. According to the World Health Organization (WHO), surface and groundwater, as well as partially treated water, containing antibiotics residue and other pharmaceuticals, typically at < 100 ng/l, whereas treated water has < 50 ng/l, respectively [22]. The discovery of ECs in numerous natural freshwater sources worldwide is growing yearly. Several antibiotic residues have been reported to have been traced at concentrations greater than their ecotoxicity endpoints in the marine environment, specifically in Europe and Africa [23]. Thus, the European Union's Water Framework Directive enumerated certain antibiotics as priority contaminants [24-26]. In some rivers, the concentrations were so high that they posed a real danger to both the ecosystem and human health. The development of effective approaches to the removal of antibiotics from the aquatic environment is of great importance.

The removal of antibiotics and their residues from water and wastewater prior to their final release into the environment is of particular concern [27]. Modern purification methods can be roughly divided into the following three categories depending on the purification mechanism: biological treatment [28,29], chemical degradation [27,30], and physical removal. Each of these methods has its own advantages and disadvantages. For example, biological purification can remove most antibiotic residues, but the introduction of active organisms into the aquatic environment can upset the ecological balance. Various chemical approaches (ozonation, chlorination, and Fenton oxidation) cannot provide complete purification and, in some cases, lead to the death of beneficial microorganisms due to low selectivity. Photocatalysis is widely used in new environmental control strategies [31-33]. This method has a number of key disadvantages, such as insufficient use of visible light, rapid annihilation of photogenerated carriers, and incomplete mineralization, which greatly limits its application [27].

Sulfonamide antibiotics (SAs) are synthetic antimicrobials derived from sulfanilic acid. Sulfamonomethoxine (SMM) is a SAs. The chemical structure of SAs is characterized by a common sulfanilamide group and a distinct 5- or 6-member heterocyclic ring [34]. The SAs have a wide spectrum of antimicrobial action against most gram-positive and numerous gram-negative microorganisms. They inhibit the proliferation of bacteria by acting as the competitive inhibitors of p-aminobenzoic acid in the folic acid metabolism cycle [35]. SAs are widely used in animal husbandry, and account for a high proportion of the total usage of antibiotics in animal therapy. SAs exhibit high excretion rates in the urine and feces of medicated animals as parent compounds or metabolites [36], and are transferred easily from contaminated sites to surrounding waters because of their low sorption to soil and sediments [35,37]. The lack of appropriate treatment for wastewater from farms for removing SA residues has resulted in the residues reaching the receiving waters surrounding the animal farms [38,39]. The SA residues have been detected in numerous aquatic environments including fish farms [40,41], their effluents and downstream waters [42-44], rivers [45,46], lakes, groundwater [47,48], and sewage wastewater [34,49]. The spread of SA residues in aquatic environments has generated great concern because of the potential risks such as enhancing microbial resistance through the prolonged exposure of microorganisms to SAs [50]. Certain SAs in

aquatic environments are potentially toxic to aquatic organisms [51].

The impetus of choosing SMM as the target contaminant stems from the fact that SMM is one of the most popular-used pharmaceuticals used for personal care products (PPCPs) but can cause serious environmental pollutions [52-54]. The facile, effective, and environment-friendly degradation of SMM-contained wastewater by a UV (365 nm)/Oxone oxidative process is reported, with presenting detailed investigations on the effects of pH values, concentrations of reagents, and reaction time within the treatment process [55]. 96.78% removal was found at 5 mg/l SMM, at λ=365 nm, after 90 min, respectively [55]. 100% removal was measured at 0.06 mM SMM, at 2.5 mM Fe_3O_4 catalyst after 15 min, respectively [56]. 98.5% photodegradation and 99% COD removal were observed at 4.53 mg/l SMM, at 0.49 mmol/l H_2O_2, at 19.51 µmol/l Fe(II), at pH=4.0 after 120 min, respectively [57]. In a research by Zhu et al. [58], iron oxide magnetic nanoparticles (Fe_3O_4 MNPs) were used to activate persulfate anions ($S_2O_8^{-2}$) to produce sulfate free radicals ($SO_4^{-\bullet}$), which are a powerful oxidant with promising applications to degrade organic contaminants. The kinetics of SMM degradation was studied in the system of Fe_3O_4 MNPs and $S_2O_8^{-2}$. A complete removal of the added SMM (0.06 mM) within 15 min with the addition of 1.20 mM $S_2O_8^{-2}$ and 2.40 mM Fe_3O_4 MNPs [56]. There was an optimum concentration of Fe_3O_4 MNPs because Fe_3O_4 MNPs may also act as a $SO_4^{-\bullet}$ scavenger at higher concentrations. Degradation mechanism of SMM on the basis of identification of the degradation intermediates was studied with liquid chromatography combined with mass spectroscopy (LC-MS) [56].

Generally, the advanced oxidation processes (AOPs), such as the Fenton or Fenton-like reaction, ozonation or catalytic ozonation, photocatalytic oxidation, electrochemical oxidation, and ionizing radiation, have been widely used for antibiotics degradation in recent years [59-63]. One of the most promising techniques applied for efficient degradation of antibiotics are AOPs [61,64-67]. Nowadays, particular attention is paid to photocatalytic reactions, in which highly oxidizing species responsible for mineralization of organic pollutants are formed in-situ in the reaction media by means of light and a photocatalyst [61,64,68,69]. The photocatalytic activity is closely related to the physicochemical properties

but also to the morphology and texture of the materials studied, for this reason the synthesis techniques are often of great importance. Photocatalysis, which occurs under exposure to UV light, is also a common method for the environmental pollutant elimination [70]. The conventional photocatalysis utilizes mostly UV from sunlight, which accounts for only 4% solar energy. Through the introduction of catalysts, the utilization rate of sunlight can be effectively improved. To overcome the low-efficiency problem of the photocatalysis, the development of a more efficient catalyst system that would effectively improve the catalytic oxidation efficiency and overcome the existing limitations is important. The catalytic activity of the catalyst can be effectively improved by modulating its surface area, preparation method, and changing its properties and structures [71-74].

Copper oxide (CuO), a p-type semiconductor with a constrained band gap (1.2-2.0 eV) and a foundation for many high-temperature superconductors and giant magnetoresistance materials, has attracted a lot of attention in recent years [75,76]. One of the attractive features of CuO NPs is that by controlling its shape and size, optical properties can be controlled. This feature is very important because it directly affects photocatalyst features. This gives importance to CuO synthesis methods because applied synthesis methods can be lead to different shapes and sizes [77-79]. Optical properties play an important role in the photocatalyst process, so here the optical properties of CuO NPs are investigated in more detail. CuO NPs have the unique ability to regulate the possible energy levels of conduction bands (CBs) and valence bands (VBs), as well as the bandgap, by adjusting the size and shape of CuO NPs. The band gap in CuO NPs is blue-shifted than bulk CuO NPs. As a result, for wider bandgap nanostructured CuO NPs samples exhibiting absorption in the UV field, CuO photocatalyst exhibits strong absorption in the visible spectrum with a little transparency [80-84]. Various techniques have been used to improve the photocatalytic properties of CuO NPs such as NCs formation, binary and ternary heterojunction formation, Z-scheme based photocatalytic system, introducing of different metal ions as dopants, and coupling with carbonaceous materials [85-90].

Zirconium dioxide (or Zircania, ZrO_2) as broad bandgap (3.25–5.1 eV) semiconductor has been widely explored due to the presence of a large

number of O_2 vacancies on the surface, significant ion exchange ability and physiochemical stability [91]. ZrO_2 NPs possesses a high value of the dielectric constant, tensile strength, melting and boiling point, however, its wide band gap and low separation rate of photogenerated electron and hole hinder the wide-scale applications [92]. To overcome this, various enhancement strategies like doping, heterojunction formation incorporation of cocatalysts, etc., have been potentially explored. For instance, Co doped ZrO_2 NCs synthesized by facile-chemical precipitation showed greater degrading activity against methylene blue dye when exposed to visible light due to the improved dielectric properties [93]. Therefore, coupling ZrO_2 NPs with narrow band semiconductors like MoS_2, TiO_2 and g-C_3N_4 also retards the photocarrier reassembly and augments its photocatalytic performance [94]. The optical properties of ZrO_2 NPs can be enhanced by introducing new electronic states by doping with rare earth metals. For example, the introduction of Ce (IV) ions in ZrO_2 NPs enhanced the photoresponse through the formation of midgap states and the Ce 4f empty states acted as a electron transfer bridge between VB and CB of ZrO_2 NPs by low energy photons [95]. Recent research has manifested that zirconia-based materials show high redox abilities, large surface area, and low thermal conductivity in PDP. In this regard, Aldeen et al. [92], comprehensively explored the altered ZrO_2 NPs based photocatalysts for organic pollutant degradation. The typical insights of inorganic pollutant degradation, specifically the heavy metal ions present in wastewater, are missing. Additionally, the importance of generating O_2 vacancies (OVs) in ZrO_2 NPs for the synergistic improvement in opto-electronic properties still needs further comprehension. Hence, the present review article highlights the features of ZrO_2 NPs semiconducting material for the photocatalytic removal of organic as well as inorganic pollutants present in wastewater. Starting from the optimal crystal structure of ZrO_2 NPs, various phases and the subsequent photocatalytic features are comprehensively reviewed. Significant methods to circumvent the inherent drawbacks of the bare ZrO_2 photocatalyst have been inclusively illustrated using different methods such as doping, heterojunction formation, morphology and structural modulation along with the formation of OVs. After this, the review introduces facile synthesis routes involving bottom-up (solvothermal, Morphology control, and doping) and top-down methods

(ultrasonication and chemical reduction) to design ZrO_2-based photocatalytic materials. Then, in order to highlight the advancement of ZrO_2 as a photocatalyst, the mechanistic insights of wastewater treatment via photocatalysis of organic and inorganic pollutants have been broadly reviewed.

CuO/ZrO_2 NCs is one of the most prominent member of CuO-based nanostructures which have been widely prepared and applied in the PDP. The physical and chemical properties of ZrO_2 NPs lead to excellent photodegradation via CuO/ZrO_2 NCs [96-98]. Nanda et al. [99] prepared CuO/ZrO_2 –MCM-41 NCs via integrating ZrO_2 into the MCM-41 (M-41) framework, then loading CuO NPs using the wetness impregnation process while maintaining a Si/Zr ratio of 10. For the photoreduction of Cr^{6+}, CuO/ZrO_2–MCM-41 was found to be an effective photocatalyst. Within 30 min, CuO/ZrO_2–MCM-41 NCs achieved at 99% reduction in Cr^{6+} [100]. CuO/ZrO_2 NCs were prepared via modified sol-gel and solid-state process. The structural and morphological properties of as-prepared samples were compared. Then, The photocatalytic H_2 evolution from oxalic acid solution under solar irradiation was used to examine the photocatalytic activity of CuO/ZrO_2 NCs. It was reported that when CuO/ZrO_2 NCs is made by sol-gel process and the mole ratio of CuO to ZrO_2 is 40%, the optimum activity of photocatalytic H_2 evolution (2.41 mmol/h.µ) is achieved [101].

In this study, CuO/ZrO_2 NCs as a photocatalys was examined during PDP in the efficient removal of Sulfamonomethoxine (SMM) from PI ww plant, İzmir, Turkey. Different pH values (3.0, 4.0, 7.0, 9.0, 10.0 and 12.0), increasing SMM concentrations (5, 10, 20 and 40 mg/l), increasing CuO/ZrO_2 NCs concentrations (100, 200, 400, 800 and 1000 mg/l), different CuO/ZrO_2 NCs mass ratios (1/2, 2/3, 3/4, 4/4, 4/3, 3/2, 2/1), increasing recycle times (1., 2., 3., 4., 5., 6. and 7.) was operated during PDP in the efficient removal of SMM in PI ww. The characteristics of the synthesized NPs were assessed using XRD, DRS, FESEM, EDX, FTIR, TEM and XPS analyses, respectively. The acute toxicity assays were operated with Microtox (*Aliivibrio fischeri*) and *Daphnia magna* acute toxicity tests. The PDP mechanisms of CuO/ZrO_2 NCs and the reaction kinetics of SMM were evaluated in PI ww during PDP. Cost analysis was evaluated for SMM removal with CuO/ZrO_2 NCs by PDP in PI ww. ANOVA statistical

analysis was used for all experimental samples.

2. MATERIALS AND METHODS

2.1 Characterization of Pharmaceutical Industry Wastewater

Characterization of the biological aerobic activated sludge proses from a PI ww plant, İzmir, Turkey was performed (Table 1).

2.2 Preparation of CuO NPs

CuO NPs were prepared as the following: First, copper sulfate ($CuSO_4$) and ammonia (NH_3) were applied as reactants. The stock solution of 0.1 M $CuSO_4$ was prepared in 100 ml deionized water. To this stock solution, aqueous NH_3 was added under continuous stirring to get the reactants at pH=9.0. The solution is next transferred into Teflon lined sealed stainless steel autoclaves and maintained at 200^oC for 6 h. It was then let to cool to 35°C. The precipitate so obtained is placed in a furnace and calcined for 2 h at 500^oC.

2.3 Synthesis of ZrO₂ NPs

In a conventional synthesis, in 100 ml distilled water 0.1 M $ZrOCl_2.8H_2O$ was dissolved with effective stirring. After a few minutes,

Table 1. Characterization of pharmaceutical ındustry wastewater (n=3, mean value)

Parameters	Unit	Concentrations
Chemical oxygen demand-total (COD_{total})	(mg/l)	4000
Chemical oxygen demand-dissolved ($COD_{dissolved}$)	(mg/l)	3200
Biological oxygen demand-5 days (BOD_5)	(mg/l)	1500
BOD_5 / $COD_{dissolved}$		0.5
Total organic carbons (TOC)	(mg/l)	1800
Dissolved organic carbons (DOC)	(mg/l)	1100
pH		8.3
Salinity as Electrical conductivity (EC)	(mS/cm)	1552
Total alkalinity as $CaCO_3$	(mg/l)	750
Total volatile acids (TVA)	(mg/l)	380
Turbidity (Nephelometric Turbidity unit, NTU)	NTU	7.2
Color	1/m	50
Total suspended solids (TSS)	(mg/l)	250
Volatile suspended solids (VSS)	(mg/l)	187
Total dissolved solids (TDS)	(mg/l)	825
Nitride (NO_2^-)	(mg/l)	1.7
Nitrate (NO_3^-)	(mg/l)	1.91
Ammonium (NH_4^+)	(mg/l)	2.3
Total Nitrogen (Total-N)	(mg/l)	3.2
Sulfite (SO_3^{-2})	(mg/l)	21.4
Sulfate (SO_4^{-2})	(mg/l)	29.3
Chloride (Cl^-)	(mg/l)	37.4
Bicarbonate (HCO_3^-)	(mg/l)	161
Phosphate (PO_4^{-3})	(mg/l)	16
Total Phosphorus (Total-P)	(mg/l)	40
Total Phenols	(mg/l)	70
Oil & Grease	(mg/l)	220
Cobalt (Co^{+3})	(mg/l)	0.2
Lead (Pb^{+2})	(mg/l)	0.4
Potassium (K^+)	(mg/l)	17
Iron (Fe^{+2})	(mg/l)	0.42
Chromium (Cr^{+2})	(mg/l)	0.44
Mercury (Hg^{+2})	(mg/l)	0.35
Zinc (Zn^{+2})	(mg/l)	0.11

0.2 M KOH is added to the above solution. Afterward, the solution formed is transferred into a stainless steel Teflon lined sterilized capacity of 100 ml and kept in an oven at 180^oC for 16 h. To remove the soluble impurities and depress agglomeration, the resulting precipitates are cleaned with distilled water and absolute ethanol (C_2H_6O). The final product was dried for 3 h in a vacuum at 80^oC.

2.4 Preparation of CuO/ZrO$_2$ NCs

The as-prepared CuO and ZrO$_2$ nanostructures were dispersed in deionized water under vigorous stirring separately. After that, the CuO NPs dispersion was added to ZrO$_2$ NPs dispersion under ultrasonic for 60 min at 25^oC. The final CuO/ZrO$_2$ NCs was filtered and dried at 60^oC for 10 h.

2.5 Photocatalytic Degradation Experiments

The photocatalytic activity of CuO/ZrO$_2$ NCs was studied against the photodegradation of SMM antibiotic under ultraviolet (UV) and visible irradiation. To attain the adsorption–desorption equilibrium, 0.03 of CuO/ZrO$_2$ NCs powder was dispersed into a 50 ml solution of SMM with the concentration of 1 mg/l, then stirred in the dark for 30 min. After then, the as-obtained suspension was exposed to the light of various wavelengths. For providing UV-Vis test, 5 ml suspensions were taken at various periods and filtered to remove the CuO/ZrO$_2$ NCs.

2.6 Photocatalytic Degradation Reactor

A 2 liter cylinder quartz glass reactor was used for the photodegradation experiments in PI ww at different operational conditions. 1000 ml PI ww was filled for experimental studies and the photocatalyst were added to the cylinder quartz glass reactors. The UV-A lamps (light intensity=147 mW/cm^2) were placed to the outside of the photo-reactor with a distance of 3 mm. The photocatalytic reactor was operated with constant stirring (1.5 rpm) during the PDP. In a typical experiment, 25 mg sample was added to 50 ml target pollutant solution. Prior to irradiation, the suspensions were stirred in dark for 100 min to reach adsorption/desorption equilibrium. 10 ml reacting solution were sampled and centrifuged at 10000 rpm, at different time intervals. The UV irradiation treatments were created using UV-A lamp emitting in λ=350–400 nm range (λ$_{max}$=368 nm;

FWHM=17 nm; Actinic BL TL-D 18W, Philips). Seven 50 W UV-A lamps (Total: 350 W UV-A lamps) were used during experimental conditions for this study. The residual concentration of organic solution in the filtrate was analyzed by using UV–vis spectrophotometer.

2.7 Characterization

2.7.1 X-Ray diffraction (XRD) analysis

Powder XRD patterns were recorded on a Shimadzu XRD-7000, Japan diffractometer using Cu Kα radiation (λ=1.5418 Å, 40 kV, 40 mA) at a scanning speed of 1° /min in the 10-80° 2θ range. Raman spectrum was collected with a Horiba Jobin Yvon-Labram HR UV-Visible NIR (200-1600 nm) Raman microscope spectrometer, using a laser with λ=512 nm. The spectrum was collected from 10 scans at a resolution of 2 /cm. The zeta potential was measured with a SurPASS Electrokinetic Analyzer (Austria) with a clamping cell at 300 mbar.

2.7.2 Field Emission Scanning Electron Microscopy (FESEM) analysis

The morphological features and structure of the synthesized catalyst were investigated by a FESEM (FESEM, Hitachi S-4700), equipped with an EDX spectrometry device (TESCAN Co., Model III MIRA) to investigate the composition of the elements present in the synthesized catalyst.

2.7.3 Energy dispersive X-Ray (EDX) spectroscopy analysis

The morphological features and structure of the synthesized catalyst were researhed by an EDX spectrometry device (TESCAN Co., Model III MIRA) to investigate the composition of the elements present in the synthesized catalyst.

2.7.4 Fourier transform ınfrared spectroscopy (FTIR) analysis

The FTIR spectra of samples was recorded using the FT-NIR spectroscope (RAYLEIGH, WQF-510).

2.7.5 Transmission electron microscopy (TEM) analysis

The structure of the samples were analysed TEM analysis. TEM analysis was recorded in a JEOL JEM 2100F, Japan under 200 kV accelerating voltage. Samples were prepared by applying one

drop of the suspended material in ethanol onto a carbon-coated copper TEM grid, and allowing them to dry at 25°C.

2.7.6 Diffuse reflectance UV-Vis spectra (DRS) analysis

DRS Analysis in λ=200–800 nm were recorded on a Cary 5000 UV-Vis Spectrophotometer from Varian.

2.7.7 X-Ray photoelectron spectroscopy (XPS) analysis

The valence state of NPs was investigated and was analyzed using XPS (ESCALAB 250Xi, England). XPS used an Al Kα source and surface chemical composition and reduction state analyses was done, with the core levels recorded using a pass energy of 30 eV (resolution ≈ 0.10 eV). The peak fitting of the individual core-levels was done using XPS-peak 41 software, achieving better fitting and component identification. All binding energies were calibrated to the C 1s peak originating from C–H or C–C groups at 284.6 eV.

2.8 Analytical Procedures

COD_{total}, $COD_{dissolved}$, Total-P, PO_4^{-3}-P, Total-N, NH_4^+-N, NO_3^--N, NO_2^--N, BOD_5, pH, T[(^{o}C)], TSS, TVSS, TOC, Oil, Cl^-, total phenol, TVA, DOC, total alkalinity, turbidity, TDS, color, SO_3^{-2}, SO_4^{-2}, HCO_3^-, salinity, Co^{+3}, Pb^{+2}, K^+, Fe^{+2}, Cr^{+2}, Hg^{+2} and Zn^{+2} were measured according to the Standard Methods (2022) 5220B, 5220D, 4500-P, 4500-PO_4^{-3}, 4500-N, 4500-NH_4^+, 4500-NO_3^-, 4500-NO_2^-, 5210B, 4500-H^+, 2320, 2540D, 2540E, 5310, 5520, 4500-Cl^-, 5530, 5560B, 5310B, 2320, 2130, 2540E, 2120, 4500-SO_3^{-2}, 4500-SO_4^{-2}, 5320, 2520, 3500-Co^{+3}, 3500-Pb^{+2}, 3500- K^+, 3500-Fe^{+2}, 3500-Cr^{+2}, 3500- Hg^{+2}, 3500-Zn^{+2}, respectively [102].

Total-N, NH_4^+-N, NO_3^--N, NO_2^--N, Total-P, PO_4^{-3}-P, total phenol, Co^{+3}, Pb^{+2}, K^+, Fe^{+2}, Cr^{+2}, Hg^{+2}, Zn^{+2}, SO_3^{-2}, and SO_4^{-2} were measured with cell test spectroquant kits (Merck, Germany) at a spectroquant NOVA 60 (Merck, Germany) spectrophotometer (2003).

The measurement of color was carried out following the methods described by Olthof and Eckenfelder [103] and Eckenfelder [104]. According these methods, the color content was determined by measuring the absorbance at three wavelengths (445, 540 and 660 nm), and taking the sum of the absorbances at these wavelengths. In order to identify the color in 25 ml PI ww was acidified at pH=2.0 with a few drops of 6 N HCl and extracted three times with 25 ml ethyl acetate. The pooled organic phases were dehydrated on sodium sulphate, filtered and dried under vacuum. The residue was sylilated with bis(trimethylsylil)trifluoroacetamide (BSTFA) in dimethylformamide and analyzed by gas chromatograph (GC) (Agilent Technology model 6890N) equipped with a mass selective (MS) detector (Agilent 5973 inert MSD) gas chromatography–mass spectrometry (GC-MS). Mass spectra were recorded using a VGTS 250 spectrometer equipped with a capillary SE 52 column (HP5-MS 30 m, 0.25 mm ID, 0.25 μm) at 220°C with an isothermal program for 10 min. The initial oven temperature was kept at 50°C for 1 min, then raised to 220°C at 25°C/min and from 200 to 300°C at 8°C/min, and was then maintained for 5.5 min. High purity He (g) was used as the carrier gas at constant flow mode (1.5 ml/min, 45 cm/s linear velocity).

The total phenol was monitored as follows: 40 ml PI ww was acidified to pH=2.0 by the addition of concentrated HCl. Total phenol was then extracted with ethyl acetate. The organic phase was concentrated at 40°C to about 1 ml and silylized by the addition of N,O-bis(trimethylsilyl) acetamide (BSA). The resulting trimethylsilyl derivatives were analysed by GC-MS (Hewlett-Packard 6980/HP5973MSD).

Methyl tertiary butyl ether (MTBE) was used to extract oil from the water and NPs. GC-MS analysis was performed on an Agilent GC system. Oil concentration was measured using a UV–vis spectroscopy fluorescence spectroscopy and a GC–MS (Hewlett-Packard 6980/HP5973MSD). UV–vis absorbance was measured on a UV–vis spectrophotometer and oil concentration was calculated using a calibration plot which was obtained with known oil concentration samples.

2.9 Acute Toxicity Assays

2.9.1 Microtox acute toxicity test

Toxicity to the bioluminescent organism *Aliivibrio fischeri (*also called *Vibrio fischeri* or *V. fischeri*) was assayed using the Microtox measuring system according to DIN 38412L34, L341, (EPS 1/ RM/24 1992). Microtox testing was performed according to the standard procedure recommended by the manufacturer [105]. A

specific strain of the marine bacterium, *V. fischeri*-Microtox LCK 491 kit [105], was used for the Microtox acute toxicity assay. Dr. LANGE LUMIX-mini type luminometer was used for the Microtox toxicity assay [106].

2.9.2 *Daphnia magna* acute toxicity test

To test toxicity, 24-h born *Daphnia magna* were used as described in Standard Methods sections 8711A, 8711B, 8711C, 8711D and 8711E, respectively [107]. After preparing the test solution, experiments were carried out using 5 or 10 *Daphnia magna* introduced into the test vessels. These vessels had 100 ml of effective volume at pH=7.0–8.0, providing a minimum DO=6 mg/l, at an ambient T=20–25°C. Young *Daphnia magna* were used in the test (≤24 h old); 24–48 h exposure is generally accepted as standard for a *Daphnia magna* acute toxicity test. The results were expressed as mortality percentage of the *Daphnia magna*. Immobile animals were reported as dead *Daphnia magna*.

2.10 Statistical Analysis

ANOVA analysis of variance between experimental data was performed to detect F and *P* values. The ANOVA test was used to test the differences between dependent and independent groups, [108]. Comparison between the actual variation of the experimental data averages and standard deviation is expressed in terms of F ratio. F is equal (found variation of the date averages/expected variation of the date averages). *P* reports the significance level, and d.f indicates the number of degrees of freedom. Regression analysis was applied to the experimental data in order to determine the regression coefficient R^2, [109]. The aforementioned test was performed using Microsoft Excel Program.

All experiments were carried out three times and the results are given as the means of triplicate samplings. The data relevant to the individual pollutant parameters are given as the mean with standard deviation (SD) values.

3. RESULTS AND DISCUSSION

3.1 Characterizations of CuO/ZrO$_2$ NCs

3.1.1 The results of X-Ray diffraction (XRD) analysis

The results of XRD analysis was observed to pure CuO NPs and pure ZrO$_2$ NPs, respectively,

in PI ww with PDP for SMM removal (Fig. 1). The characterization peaks of pure CuO NPs were observed at 2θ values and corresponding of 30.05^{o} (110), 33.19^{o} (002), 37.18^{o} (111), 39.75^{o} (202), 48.11^{o} (020), 59.07^{o} (202), 62.58^{o} (113), 67.80^{o} (311) and $75.12°$ (220), respectively, in PI ww with PDP for SMM removal (Fig. 1a). The characterization peaks of pure ZrO$_2$ NPs were obtained at 2θ values and corresponding of 30.04^{o} (110), 32.79^{o} (011), 43.52^{o} (110), 50.59^{o} (111), 59.17^{o} (002), 61.78^{o} (200), 65.24^{o} (211) and 74.37^{o} (220), respectively, in PI ww with PDP for SMM removal (Fig. 1b).

3.1.2 The results of diffuse reflectance UV-Vis Spectra (DRS) analysis

The absorption spectra of SMM was observed in DRS Analysis (Fig. 2). First, the absorption spectra of SMM were obtained at maximum 1600 mg/l in the λ=200-600 nm using diffuse reflectance UV-Vis spectra (Fig. 2). Absorption peaks were observed at λ=225 nm for CuO/ZrO$_2$ NCs, respectively, in PI ww with PDP for SMM removal (Fig. 2).

3.1.3 The results of field emission scanning electron microscopy (FESEM) analysis

The morphological features of pure CuO NPs, pure ZrO$_2$ NPs and CuO/ZrO$_2$ NCs were characterized through FESEM images (Fig. 3). The FESEM images of pure CuO NPs (Fig. 3a), pure ZrO$_2$ NPs (Fig. 3b) and CuO/ZrO$_2$ NCs (Fig. 3c) were characterized in PI ww with PDP for SMM removal.

3.1.4 The results of energy dispersive X-Ray (EDX) spectroscopy analysis

The EDX analysis was also performed to investigate the composition of CuO/ZrO$_2$ NCs in PI ww with PDP for SMM removal (Fig. 4).

3.1.5 The results of fourier transform ınfrared spectroscopy (FTIR) analysis

The FTIR spectrum of CuO/ZrO$_2$ NCs in PI ww with PDP for SMM removal (Fig. 5). The main peaks of FTIR spectrum for CuO/ZrO$_2$ NCs was observed at 3475 cm^{-1}, 1051 cm^{-1}, 627 cm^{-1} and 512 cm^{-1} wavenumber, respectively (Fig. 5).

3.1.6 The results of transmission electron microscopy (TEM) analysis

The TEM images of CuO/ZrO$_2$ NCs was observed in micromorphological structure level in PI ww with PDP for SMM removal (Fig. 6).
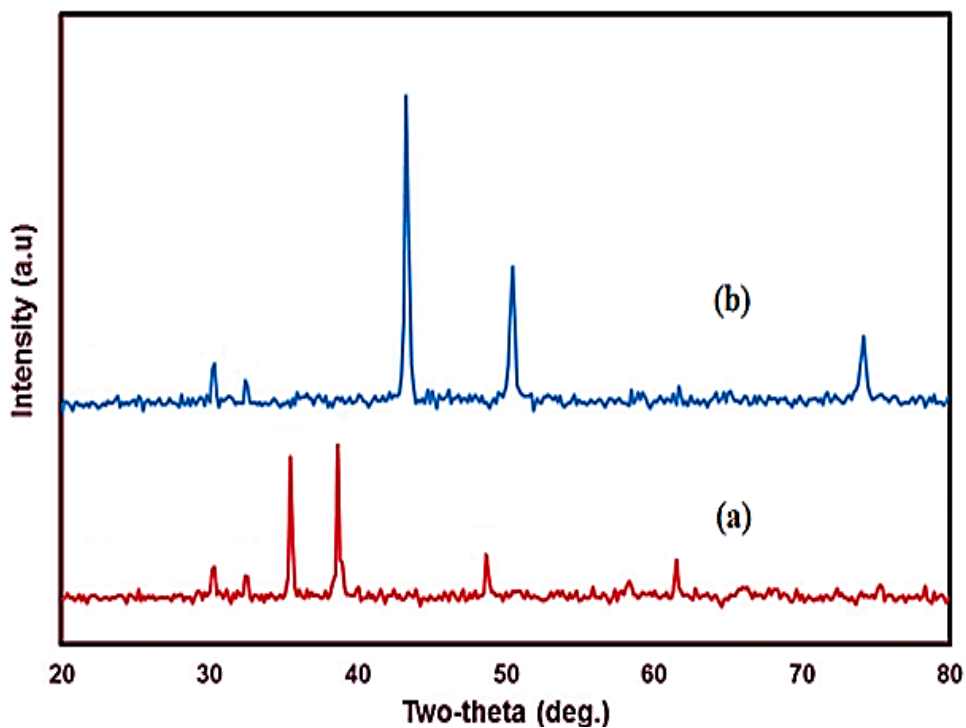
Fig. 1. The XRD patterns of (a) pure CuO NPs (red pattern) and (b) pure ZrO$_2$ NPs (blue pattern), respectively, in PI ww with PDP for SMM removal
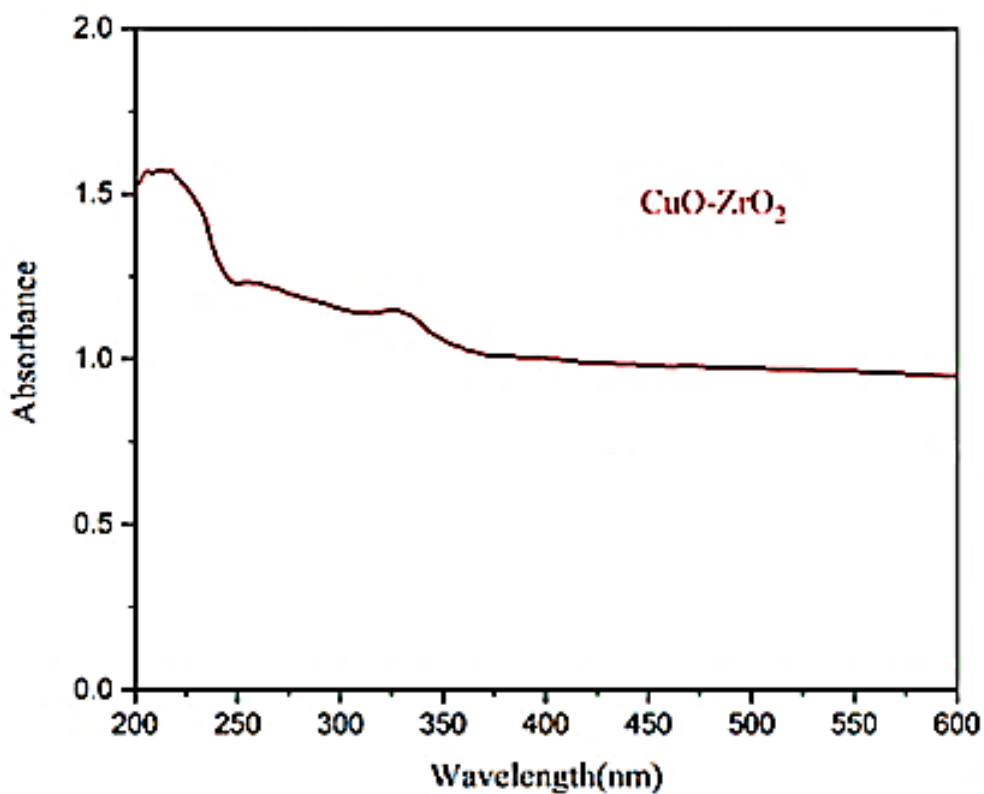

Fig. 2. The DRS patterns of CuO/ZrO$_2$ NCs in PI ww with PDP for SMM removal
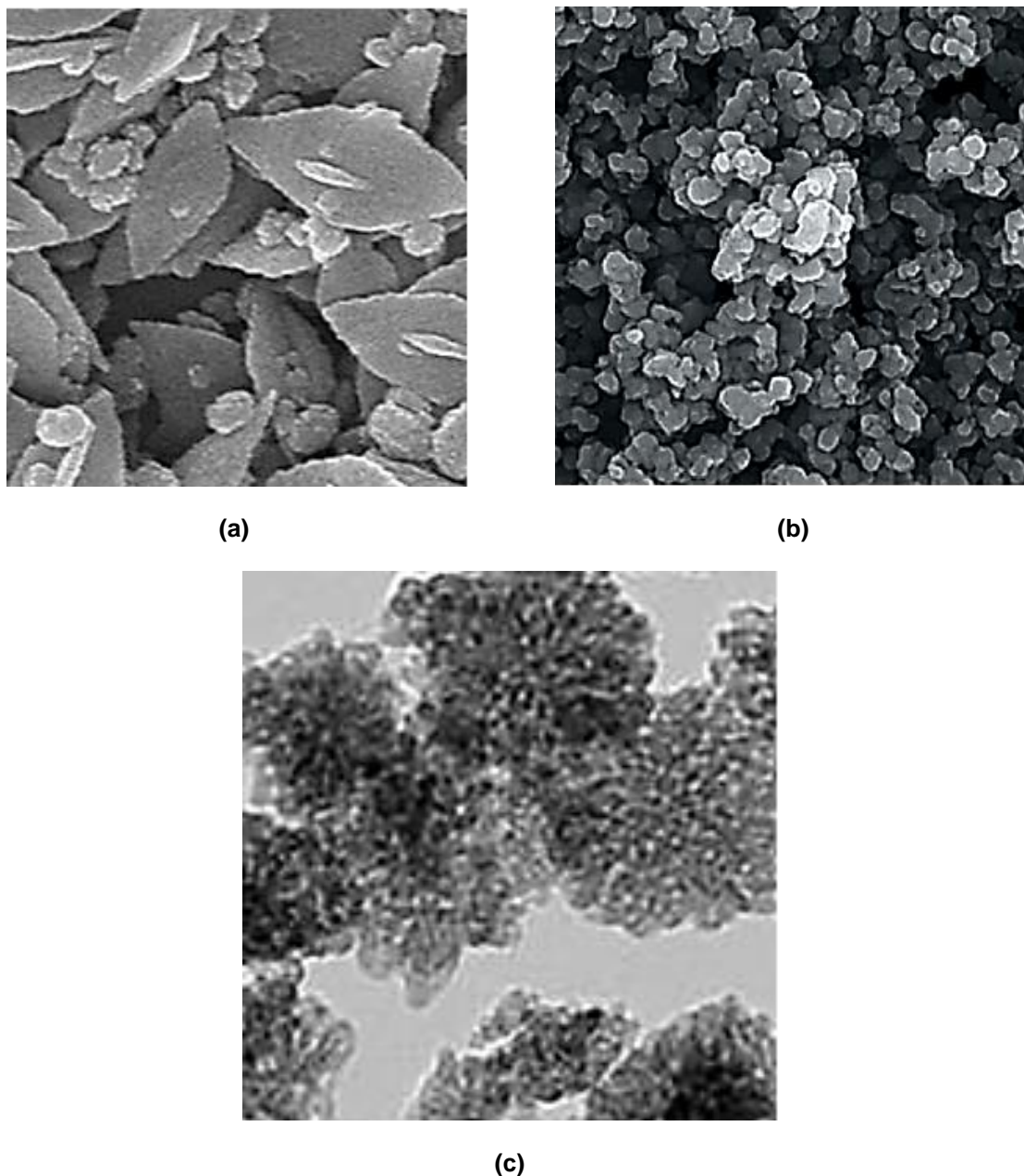
(a)

(b)

(c)

Fig. 3. FESEM images of (a) pure CuO NPs, (b) pure ZrO$_2$ NPs and (c) CuO/ZrO$_2$ NCs, respectively, in PI ww with PDP for SMM removal. (FESEM images scale: 200 nm)

3.1.7 X-Ray photoelectron spectroscopy (XPS) analysis

The XPS analysis of CuO/ZrO$_2$ NCs in micromorphological structure level in PI ww with PDP for SMM removal (Fig. 7).

3.2 The Reaction Kinetics of SMM Antibiotic

The reaction kinetics SMM were investigated using the Langmuir–Hinshelwood first-order kinetic model, expressed by Eddy et al. [110], as following **Equation (1):**

$$r_o = -\frac{dC}{dt} = kC \qquad (1)$$

where; r_o: denotes the initial photocatalytic degradation reaction rate (mg/l.min), and k: denotes the rate constant of a first-order reaction. At the beginning of the reaction, t = 0, C_t = C_0, the equation can be obtained after integration as following **Equation (2):**

$$ln\frac{C}{C_0} = -kt \qquad (2)$$

where; C_0 and C : are the initial and final concentration (mg/l) of SMM; the solution at t (min) and k (1/min) are the rate constant.
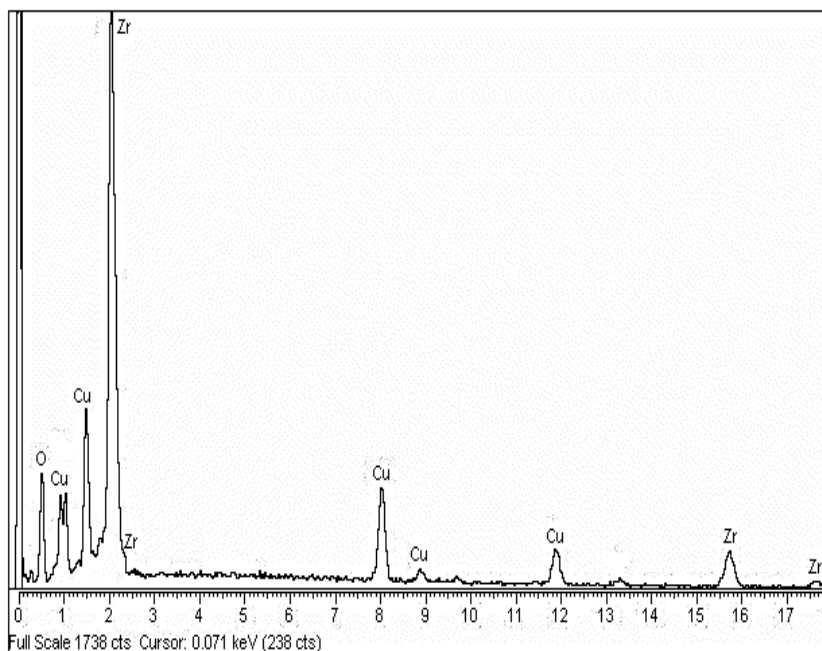
The correlation coefficients had R^2 values greater than 0.9, as a result, the first-order kinetic model fit the experimental data well. The first-order rate constants (k) were determined from the slope of the linear plots.

Fig. 4. EDX spectrum of CuO/ZrO$_2$ NCs, respectively, in PI ww with PDP for SMM removal
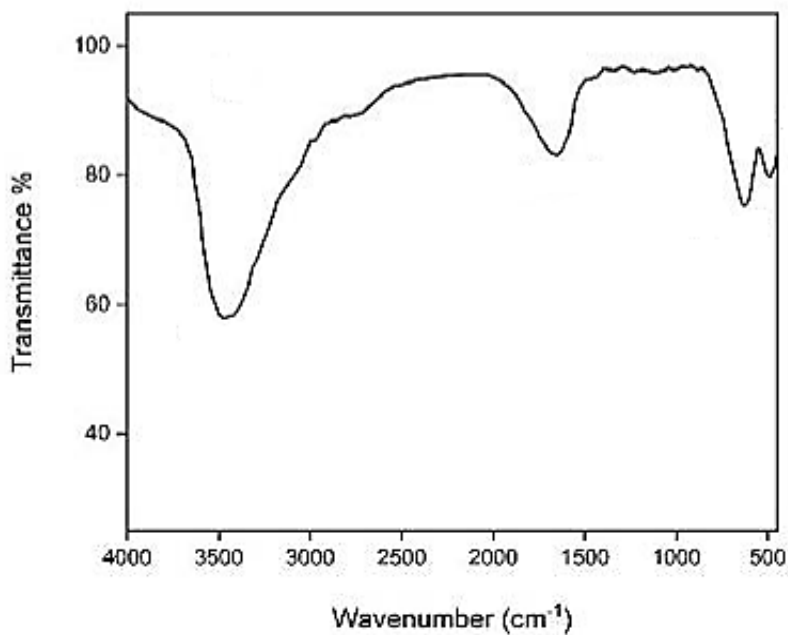

Fig. 5. FTIR spectrum of CuO/ZrO$_2$ NCs in PI ww with PDP for SMM removal
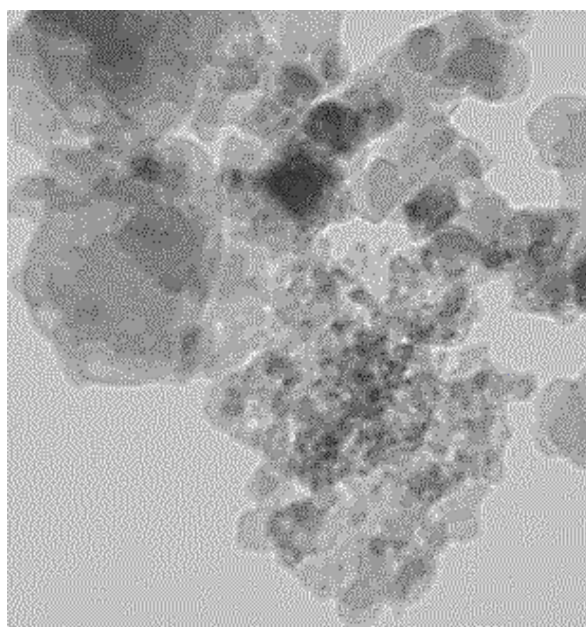
Fig. 6. TEM images of CuO/ZrO$_2$ NCs in micromorphological structure level in PI ww with PDP for SMM removal. (TEM images scale: 200 nm)
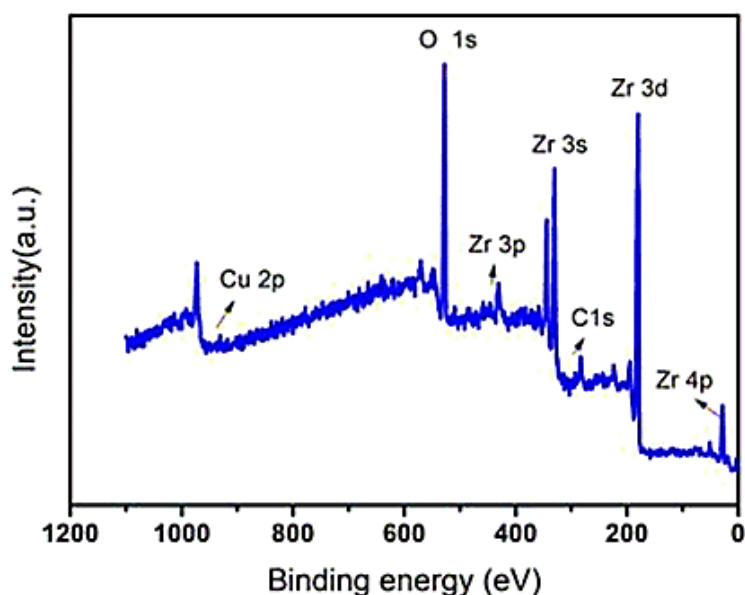

Fig. 7. XPS spectra of CuO/ZrO$_2$ NCs in micromorphological structure level in PI ww with PDP for SMM removal

3.3 Photocatalytic Degradation Mechanisms

The photocatalytic performance of the catalyst in the degradation of SMM is determined by photons. The degradation mechanism of SMM by hydroxyl radicals (OH$^\bullet$) radicals concerning CuO/ZrO$_2$ NCs as following equations (**Equation 3, Equation 4, Equation 5, Equation 6,** **Equation 7, Equation 8, Equation 9** and **Equation 10**):

$$CuO/ZrO_2 + hv \rightarrow CuO\ (h^+ + e^-)/ZrO_2\ (h^+ + e^-) \tag{3}$$

$$CuO\ (h^+ + e^-)/ZrO_2\ (h^+ + e^-) \rightarrow CuO\ (h^+ + h^+)/ZrO_2\ (e^- + e^-) \tag{4}$$

$$e^- + O_2 \rightarrow O_2^{-\bullet} \tag{5}$$

$$h^+ + H_2O \rightarrow OH^\bullet + h^+ \tag{6}$$

$$ZrO_2(h^+) + H_2O \rightarrow OH^\bullet + H^+ + ZrO_2 \tag{7}$$

$$OH^- + ZrO_2(h^+) \rightarrow OH^\bullet + ZrO_2 \tag{8}$$

$$O_2 + e^- \rightarrow O_2^{-\bullet} \tag{9}$$

$$SMM + O_2^{-\bullet}/OH^\bullet \rightarrow$$
$$CO_2 + H_2O + Degradation\ Products \tag{10}$$
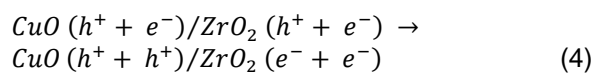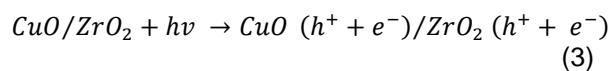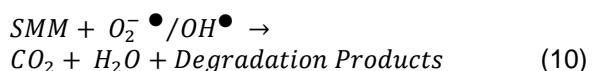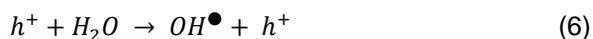
CuO/ZrO_2 NCs absorbs photons with energies greater than the photocatalyst bandgap. As a result, the electron in the VB jumps to the CB, leaving a hole in the CB. The electrons present in the CB and VB will react with O_2 and H_2O molecules which are absorbed by the photocatalyst and lead to the formation of $OH^\bullet$ radicals which react with SMM. $OH^\bullet$ radicals are produced when the photocatalyst surface is illuminated with photons, and $OH^\bullet$ radicals are strong oxidising species, with an oxidation potential of approximately 2.8 V [as opposed to Normal hydrogen electrode (NHE)], which may increase total pollutant mineralisation. Normally, the higher the rate of formation of $OH^\bullet$ radicals, the greater the separation efficiency of electron-hole pairs. In this way, there is a correlation between the increased photocatalytic activity and the rate of formation of $OH^\bullet$ radicals. The $OH^\bullet$ radicals generation of CuO/ZrO_2 NCs was extremely high, indicating that the sample has a high electron and hole separation rate.

3.4 Effect of Increasing pH Values for SMM Removal in PI ww during PDP

Increasing pH values (pH=3.0, pH=4.0, pH=7.0, pH=9.0, pH=10.0 and pH=12.0, respectively) was examined during PDP in PI ww for SMM removal, at 350 W UV-vis, at 147 mW/cm^2, after 120 min and at 25^oC, respectively (Fig. 8). 52.2%, 75.7%, 80.4%, 87.5% and 95.8% SMM removal was measured at pH=3.0, pH=4.0, pH=7.0, pH=9.0 and pH=10.0, respectively, at 350 W UV-vis, at 147 mW/cm^2, after 120 min and at 25^oC, respectively (Fig. 8). The maximum 99.6% SMM removal was obtained during PDP in PI ww, at 350 W UV-vis, at 147 mW/cm^2, after 120 min, at pH=12.0 and at 25^oC, respectively (Fig. 8).

3.5 Effect of Increasing SMM Concentrations for SMM Removal in PI ww during PDP

Increasing SMM concentrations (5, 10, 20 and 40 mg/l) were operated at 350 W UV-vis, at 147 mW/cm^2, after 120 min, at pH=12.0 and at 25^oC, respectively (Fig. 9). 90.3%, 82.1% and 59.7% SMM removals were obtained to 10, 20 and 40 mg/l SMM concentrations, at 350 W UV-vis, at 147 mW/cm^2, after 120 min, at pH=12.0 and at 25^oC, respectively (Fig. 9). The maximum 99.2% SMM removal was found with PDP in PI ww, at 5 mg/l SMM, at 350 W UV-vis, at 147 mW/cm^2, after 120 min, at pH=12.0 and at 25^oC, respectively (Fig. 9).
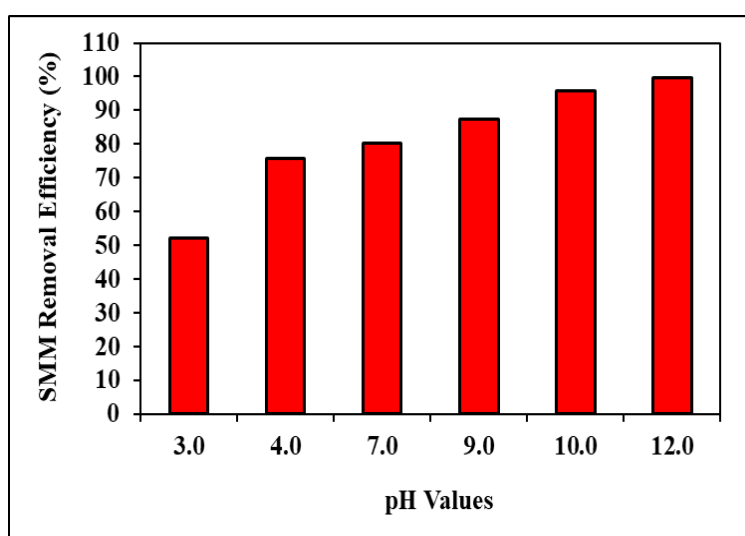

Fig. 8. Effect of increasing pH values for SMM removal in PI ww during PDP, at 350 W UV-vis, at 147 mW/cm^2, after 120 min and at 25^oC, respectively
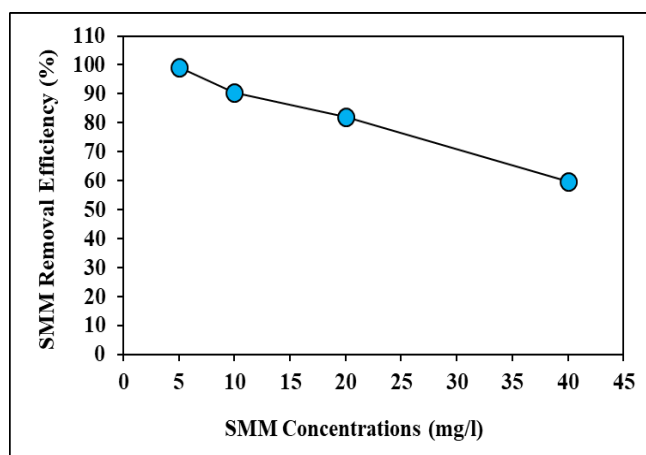
Fig. 9. Effect of increasing SMM concentrations for SMM removal in PI ww during PDP, at 350 W UV-vis, at 147 mW/cm^2, after 120 min, at pH=12.0 and at 25°C, respectively
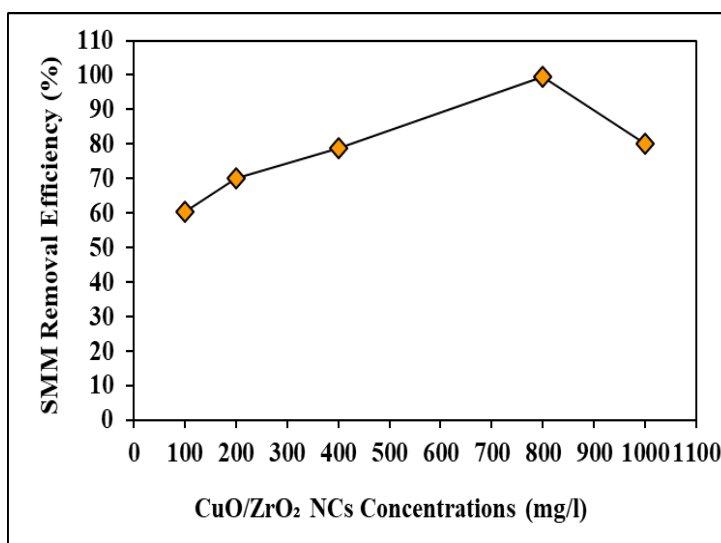

Fig. 10. Effect of increasing CuO/ZrO$_2$ NCs concentrations for SMM removal in PI ww during PDP, at 5 mg/l SMM, at 350 W UV-vis, at 147 mW/cm^2, after 120 min, at pH=12.0 and at 25°C, respectively

3.6 Effect of Increasing CuO/ZrO$_2$ NCs Concentrations for SMM Removals in PI ww during PDP

Increasing CuO/ZrO$_2$ NCs concentrations (100, 200, 400, 800 and 1000 mg/l) were operated at 5 mg/l SMM, at 350 W UV-vis, at 147 mW/cm^2, after 120 min, at pH=12.0 and at 25°C, respectively (Fig. 10). 60.5%, 70.1%, 78.8% and 80.1% SMM removals were obtained to 100, 200, 400 and 1000 mg/l CuO/ZrO$_2$ NCs concentrations, respectively, at 5 mg/l SMM, at 350 W UV-vis, at 147 mW/cm^2, after 120 min, at pH=12.0 and at 25°C, respectively (Fig. 10). The maximum 99.5% SMM removal was measured to

800 mg/l CuO/ZrO$_2$ NCs with PDP in PI ww, at 5 mg/l SMM, at 350 W UV-vis, at 147 mW/cm^2, after 120 min, at pH=12.0 and at 25°C, respectively (Fig. 10).

3.7 Effect of Different CuO/ZrO$_2$ NCs Mass Ratios for SMM Removals in PI ww during PDP

Different CuO/ZrO$_2$ mass ratios (1/2wt, 2/3wt, 3/4wt, 4/4wt, 4/3wt, 3/2 and 2/1wt, respectively) were examined for SMM removal in PI ww during PDP, at 5 mg/l SMM, at 800 mg/l CuO/ZrO$_2$ NCs, at 350 W UV-vis, at 147 mW/cm^2, after 120 min, at pH=12.0 and at 25°C, respectively (Fig. 11).

47.3%, 53.6%, 68.9%, 84.7%, 73.1% and 59.2% SMM removals were measured at 1/2wt, 2/3 wt, 3/4wt, 4/4wt, 3/2 and 2/1wt CuO/ZrO_2 NCs mass ratios, respectively, at 5 mg/l SMM, at 800 mg/l CuO/ZrO_2 NCs, at 350 W UV-vis, at 147 mW/cm^2, after 120 min, at pH=12.0 and at 25^oC, respectively (Fig. 11). The maximum 99.4% SMM removal was measured at 4/3wt CuO/ZrO_2 NCs mass ratios, at 5 mg/l SMM, at 800 mg/l CuO/ZrO_2 NCs, at 350 W UV-vis, at 147 mW/cm^2, after 120 min, at pH=12.0 and at 25^oC, respectively (Fig. 11).

3.8 Effect of Different Recycle Times for SMM Removals in PI ww during PDP

Different recycle times (1., 2., 3., 4., 5., 6. and 7.) were operated for SMM removals in PI ww during PDP, at 5 mg/l SMM, at 800 mg/l CuO/ZrO_2 NCs, at 4/3wt CuO/ZrO_2 NCs mass rartio, at 350 W UV-vis, at 147 mW/cm^2, after 120 min, at pH=12.0 and at 25^oC, respectively (Fig. 12). 92.6%, 85.2%, 77.8%, 73.2%, 68.6% and 64.1% SMM recovery yields were measured after 2. recycle time, 3. recycle time, 4. recycle time, 5. recycle time, 6. recycle time and 7. recycle time, respectively, at 5 mg/l SMM, at 800 mg/l CuO/ZrO_2 NCs, at 4/3wt CuO/ZrO_2 NCs mass

rartio, at 350 W UV-vis, at 147 mW/cm^2, after 120 min, at pH=12.0 and at 25^oC, respectively (Fig. 12). The maximum 99.5% SMM recovery was measured in PI ww during PDP, after 1. recycle time, at 5 mg/l SMM, at 800 mg/l CuO/ZrO_2 NCs, at 4/3wt CuO/ZrO_2 NCs mass rartio, at 350 W UV-vis, at 147 mW/cm^2, after 120 min, at pH=12.0 and at 25^oC, respectively (Fig. 12).

3.9 Acute Toxicity Assays

3.9.1 Effect of ıncreasing SMM concentrations on the microtox acute toxicity removal efficiencies in PI ww at ıncreasing photocatalytic degradation time and temperature

In Microtox with *Aliivibrio fischeri* (*Vibrio fischeri*) acute toxicity test, the initial EC_{90} values at pH=7.0 was found as 825 mg/l at 25^oC (Table 2: SET 1). After 60, 120 and 180 min photocatalytic degradation time, the EC_{90} values decreased to EC_{57}=414 mg/l to EC_{22}=236 mg/l and to EC_{12}=165 mg/l in SMM=20 mg/l at 30^oC (Table 2: SET 3). The Microtox acute toxicity removals were 41.75%, 80.64% and 91.75% after 60, 120 and 180 min, respectively, in SMM=20 mg/l and at 30^oC (Table 2: SET 3).
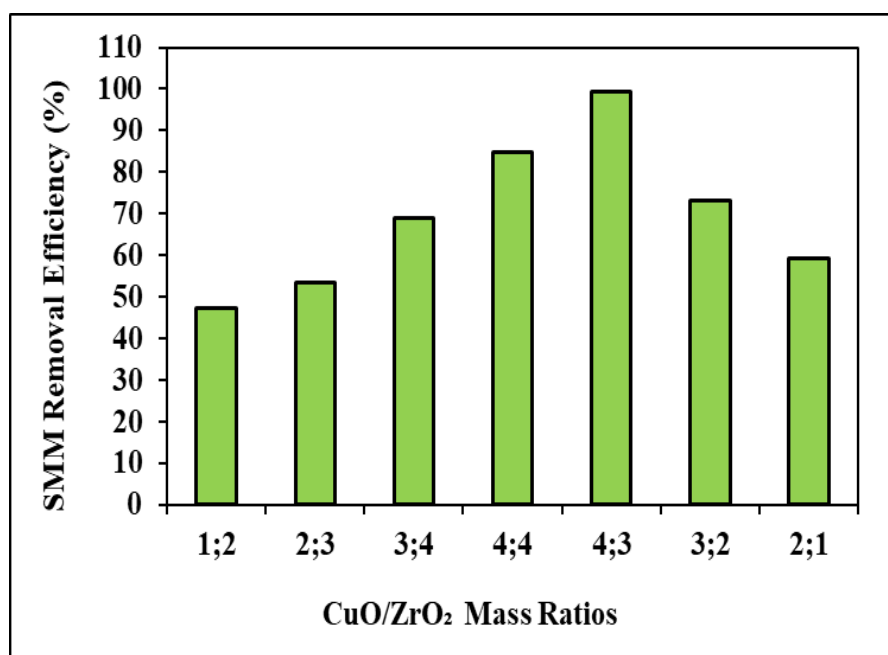

Fig. 11. Effect of different CuO/ZrO_2 NCs mass ratios for SMM removal in PI ww during PDP, at 5 mg/l SMM, at 800 mg/l CuO/ZrO_2 NCs, at 350 W UV-vis, at 147 mW/cm^2, after 120 min, at pH=12.0 and at 25^oC, respectively

Table 2. Effect of increasing SMM concentrations on Microtox acute toxicity in PI ww after PDP, at 30°C and at 60°C, respectively

No	Parameters	Microtox Acute Toxicity Values, * EC (mg/l)							
		25°C							
		0. min		60. min		120. min		180. min	
		*EC$_{90}$		*EC		*EC		*EC	
1	Raw ww, control	825		EC$_{70}$=510		EC$_{60}$=650		EC$_{49}$=638	
		30°C				60°C			
		0. min	60. min	120. min	180. min	0. min	60. min	120. min	180. min
		*EC$_{90}$	*EC	*EC	*EC	*EC$_{90}$	*EC	*EC	*EC
2	Raw ww, control	825	EC$_{70}$=580	EC$_{50}$= 580	EC$_{39}$=548	825	EC$_{55}$= 550	EC$_{40}$= 590	EC$_{29}$=688
3	SMM=5 mg/l	825	EC$_{63}$=421	EC$_{28}$=241	EC$_{18}$=167	825	EC$_{58}$=418	EC$_{23}$=265	EC$_{13}$=149
	SMM=10 mg/l	825	EC$_{62}$=420	EC$_{27}$=238	EC$_{17}$=166	825	EC$_{57}$=413	EC$_{22}$=231	EC$_{12}$=160
	SMM=20 mg/l	825	EC$_{58}$ =413	EC$_{23}$=235	EC$_{13}$=164	825	EC$_{53}$=549	EC$_{18}$=539	EC$_{8}$=499
	SMM=40 mg/l	825	EC$_{68}$=407	EC$_{33}$=229	EC$_{23}$=161	825	EC$_{63}$=402	EC$_{28}$=217	EC$_{18}$=147

* EC values were calculated based on COD$_{dis}$ (mg/l)

Table 3. Effect of increasing SMM concentrations on *Daphnia magna* acute toxicity in PI ww after PDP, at 30°C and at 60°C

No	Parameters	*Daphnia magna* Acute Toxicity Values, * EC (mg/l)							
		25°C							
		0. min		60. min		120. min		180. min	
		*EC$_{50}$		*EC		*EC		*EC	
1	Raw ww, control	850		EC$_{45}$=625		EC$_{40}$=370		EC$_{29}$=153	
		30°C				60°C			
		0. min	60. min	120. min	180. min	0. min	60. min	120. min	180. min
		*EC$_{50}$	*EC	*EC	*EC	*EC$_{50}$	*EC	*EC	*EC
2	Raw ww, control	850	EC$_{39}$=468	EC$_{34}$=228	EC$_{23}$=111	850	EC$_{34}$=373	EC$_{29}$=210	EC$_{18}$=71
3	SMM=5 mg/l	850	EC$_{33}$=449	EC$_{23}$=144	EC$_{18}$=259	850	EC$_{33}$=129	EC$_{18}$=424	EC$_{13}$=339
	SMM=10 mg/l	850	EC$_{37}$=449	EC$_{22}$=174	EC$_{17}$=99	850	EC$_{32}$=424	EC$_{17}$=139	EC$_{7}$=89
	SMM=20 mg/l	850	EC$_{33}$=349	EC$_{18}$=239	EC$_{13}$=89	850	EC$_{28}$=149	EC$_{13}$=59	EC8=374
	SMM=40 mg/l	850	EC$_{43}$=299	EC$_{28}$=169	EC$_{23}$=51	850	EC$_{38}$=249	EC$_{23}$=109	EC$_{18}$=10

* EC values were calculated based on COD$_{dis}$ (mg/l)

Table 4. The responses of Microtox and *Daphnia magna* acute toxicity tests in addition of increasing SMM concentrations without PI ww during PDP after 180 min, at 25°C

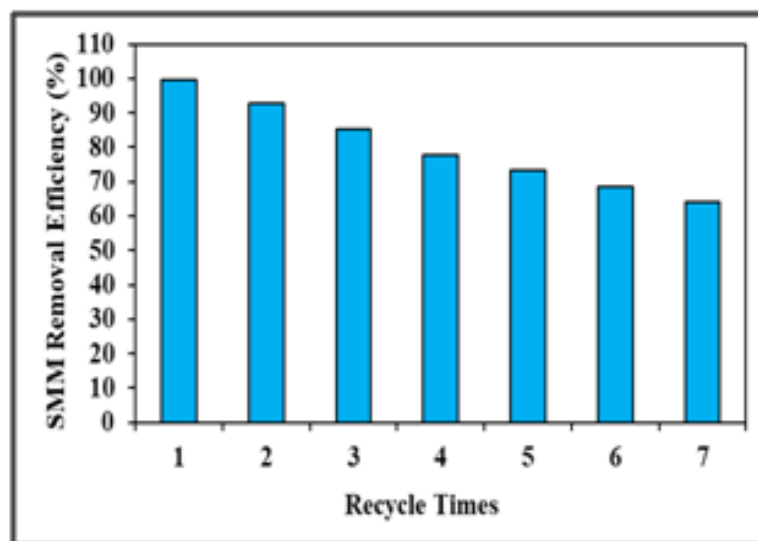| SMM Conc. (mg/l)	Microtox Acute Toxicity Test			*Daphnia magna* Acute Toxicity Test		
	Initial EC$_{50}$ value (mg/l)	Inhibitions after 180 min	EC Values (mg/l)	Initial EC$_{50}$ value (mg/l)	Inhibitions after 180 min	EC values (mg/l)
5	EC$_{11}$=23	-	-	EC$_{11}$=38	-	-
10	EC$_{15}$=78	3	EC$_2$=3	EC$_{20}$=98	5	EC$_3$=4
20	EC$_{21}$=148	6	EC$_4$=6	EC$_{31}$=198	7	EC$_7$=10
40	EC$_{26}$= 218	8	EC$_6$=9	EC$_{41}$=298	10	EC$_9$=14

Fig. 12. Effect of recycle times for SMM removal in PI ww during PDP, at 5 mg/l SMM, at 800 mg/l CuO/ZrO$_2$ NCs, at 4/3wt CuO/ZrO$_2$ NCs mass rartio, at 350 W UV-vis, at 147 mW/cm^2, after 120 min, at pH=12.0 and at 25°C, respectively

The EC_{90} values decreased to EC_{53}, to EC_{18} and to EC_8 after 60, 120 and 180 min, respectively, in SMM=20 mg/l, at 60°C (Table 2: SET 3). The EC_{51}=549 mg/l, EC_{11} =539 mg/l and EC_7=499 mg/l values were measured in SMM=20 mg/l, at 60°C. The toxicity removals were 47.30%, 86.29% and 97.31% after 60, 120 and 180 min, respectively, in SMM=20 mg/l, at 60°C (Table 2: SET 3). 97.31% maximum Microtox acute toxicity removal was found in SMM=20 mg/l after 180 min and at 60°C (Table 2: SET 3).

The EC_{90} values decreased to EC_{63}=421 mg/l to EC_{28}=241 mg/l and to EC_{18}=167 mg/l after 60, 120 and 180 min, respectively, in SMM=5 mg/l at 30°C (Table 2: SET 3). The EC_{90} values decreased to EC_{62}=420 mg/l to EC_{27}=238 mg/l and to EC_{11}=166 mg/l after 60, 120 and 180 min, respectively, in SMM=10 mg/l at 30°C. The EC_{90} values decreased to EC_{68}=407 mg/l to EC_{33}=229 mg/l and to EC_{23}=161 mg/l after 60, 120 and 180 min, respectively, in SMM=40 mg/l at 30°C. The Microtox acute toxicity removals were 86.19%, 86.17% and 80.64% in 5, 10 and 40 mg/l SMM, respectively, after 180 min, at 30°C. It was obtained an inhibition effect of SMM=40 mg/l to *Vibrio fischeri* after 180 min and at 30°C (Table 2: SET 3).

The EC_{90} values decreased to EC_{58}=418 mg/l to EC_{23}=265 mg/l and to EC_{13}=149 mg/l after 60, 120 and 180 min, respectively, in SMM=5 mg/l at 60°C (Table 2: SET 3). The EC_{90} values decreased to EC_{57}=413 mg/l to EC_{22}=231 mg/l and to EC_{12}=160 mg/l after 60, 120 and 180 min, respectively, in SMM=10 mg/l at 60°C. The EC_{90} values decreased to EC_{63}=402 mg/l to EC_{28}=217 mg/l and to EC_{18}=147 mg/l after 60, 120 and 180 min, respectively, in SMM=40 mg/l at 60°C. The Microtox acute toxicity removals were 91.75%, 91.72% and 86.21% in 5, 10 and 40 mg/l SMM, respectively, after 180 min, at 60°C. It was observed an inhibition effect of SMM=40 mg/l to Microtox with *Vibrio fischeri* after 180 min, and at 60°C (Table 2: SET 3).

3.9.2 Effect of increasing SMM concentrations on the *daphnia magna* acute toxicity removal efficiencies in PI ww at ıncreasing photocatalytic degradation time and temperature

The initial EC_{50} values were observed as 850 mg/l at 25°C (Table 3: SET 1). After 60, 120 and 180 min, the EC_{50} values decreased to EC_{32}=349 mg/l to EC_{18}=239 mg/l and to EC_{13}=89 mg/l in SMM=20 mg/l, at 30°C (Table 3: SET 3). The

toxicity removals were 43.85%, 73.76% and 83.54% after 60, 120 and 180 min, respectively, in SMM=20 mg/l at 30°C (Table 3: SET 3).

The EC_{50} values decreased to EC_{28} to EC_{13} and to EC_8 after 60, 120 and 180 min, respectively, in SMM=20 mg/l at 60°C (Table 3: SET 3). The EC_{28}=149 mg/l, EC_{13}=59 mg/l and EC_8=374 mg/l values were measured in SMM=20 mg/l at 60°C. The toxicity removals were 53.83%, 83.51% and 93.27% after 60, 120 and 180 min, respectively, in SMM=20 mg/l at 60°C (Table 3: SET 3). 93.27% maximum *Daphnia magna* acute toxicity removal was obtained in SMM=20 mg/l after 180 min and at 60°C, respectively (Table 3: SET 3).

The EC_{50} values decreased to EC_{38}=449 mg/l to EC_{23}=144 mg/l and to EC_{18}=259 mg/l after 60, 120 and 180 min, respectively, in SMM=5 mg/l at 30°C (Table 3: SET 3). The EC_{50} values decreased to EC_{37}=449 mg/l to EC_{22}=174 mg/l and to EC_{17}=99 mg/l after 60, 120 and 180 min, respectively, in SMM=10 mg/l and at 30°C. The EC_{50} values decreased to EC_{43}=299 mg/l to EC_{28}=169 mg/l and to EC_{23}=51 mg/l after 60, 120 and 180 min, respectively, in SMM=40 mg/l and at 30°C. The *Daphnia magna* acute toxicity removals were 73.11%, 73.45% and 64.10% in 5, 10 and 40 mg/l SMM, respectively, after 180 min and at 30°C. It was observed an inhibition effect of SMM=40 mg/l to *Daphnia magna* after 180 min and at 30°C (Table 3: SET 3).

The EC_{50} values decreased to EC_{33}=129 mg/l to EC_{18}=424 mg/l and to EC_{13}=339 mg/l after 60, 120 and 180 min, respectively, in SMM=5 mg/l and at 60°C (Table 3: SET 3). The EC_{50} values decreased to EC_{32}=424 mg/l to EC_{17}=139 mg/l and to EC_7=89 mg/l after 60, 120 and 180 min, respectively, in SMM=10 mg/l and at 60°C. The EC_{50} values decreased to EC_{38}=249 mg/l to EC_{23}=109 mg/l and to EC_{18}=10 mg/l after 60, 120 and 180 min, respectively, in SMM=40 mg/l and at 60°C. The *Daphnia magna* acute toxicity removals were 84.95%, 93.54% and 74.22% in 5, 10 and 40 mg/l SMM, respectively, after 180 min and at 60°C. It was observed an inhibition effect of SMM=40 mg/l to *Daphnia magna* after 180 min and at 60°C (Table 3: SET 3).

Increasing the SMM concentrations from 5 to 40 mg/l did not have a positive effect on the decrease of EC_{50} values as shown in Table 3 at SET 3. SMM concentrations > 20 mg/l decreased the acute toxicity removals by hindering the PDP. Similarly, a significant contribution of increasing SMM concentration to acute toxicity removal at

60°C after 180 min was not observed. Low toxicity removals found at high SMM concentrations could be attributed to their detrimental effect on the *Daphnia magna* (Table 3: SET 3).

3.9.3 Direct effects of SMM concentrations on the acute toxicity of microtox and *Daphnia magna* without PI ww after PDP

The acute toxicity test was performed in the samples containing 5, 10, 20 and 40 mg/l SMM concentrations, at 25°C. In order to detect the direct responses of Microtox and *Daphnia magna* to the increasing SMM concentrations the toxicity test were performed without PI ww after PDP, at 25°C. The initial EC values and the EC_{50} values were measured in the samples containing increasing SMM concentrations after 180 min. Table 4 showed the responses of Microtox and *Daphnia magna* to increasing SMM concentrations.

The acute toxicity originating only from 5, 10, 20 and 40 mg/l SMM were found to be low (Table 4). 5 mg/l SMM did not exhibited toxicity to *Aliivibrio fischeri* and *Daphnia magna* before and after 180 min. The toxicity atributed to the 10, 20 and 40 mg/l SMM were found to be low in the samples without PI ww after PDP for the test organisms mentioned above. The acute toxicity originated from the SMM decreased significantly to EC_2, EC_4 and EC_6 after 180 min. Therefore, it can be concluded that the toxicity originating from the SMM is not significant and the real acute toxicity throughout PDP was attributed to the PI ww, to their metabolites and to the photocatalytic degradation by-products (Table 4).

4. CONCLUSIONS

The maximum 99.6% SMM removal was obtained during PDP in PI ww, at 350 W UV-vis, at 147 mW/cm^2, after 120 min, at pH=12.0 and at 25°C, respectively.

The maximum 99.2% SMM removal was found with PDP in PI ww, at 5 mg/l SMM, at 350 W UV-vis, at 147 mW/cm^2, after 120 min, at pH=12.0 and at 25°C, respectively.

The maximum 99.5% SMM removal was measured to 800 mg/l CuO/ZrO$_2$ NCs with PDP in PI ww, at 5 mg/l SMM, at 350 W UV-vis, at 147 mW/cm^2, after 120 min, at pH=12.0 and at 25°C, respectively.

The maximum 99.4% SMM removal was measured at 4/3wt CuO/ZrO$_2$ NCs mass ratios, at 5 mg/l SMM, at 800 mg/l CuO/ZrO$_2$ NCs, at 350 W UV-vis, at 147 mW/cm^2, after 120 min, at pH=12.0 and at 25°C, respectively.

The maximum 99.5% SMM recovery was measured in PI ww during PDP, after 1. recycle time, at 5 mg/l SMM, at 800 mg/l CuO/ZrO$_2$ NCs, at 4/3wt CuO/ZrO$_2$ NCs mass rartio, at 350 W UV-vis, at 147 mW/cm^2, after 120 min, at pH=12.0 and at 25°C, respectively.

97.31% maximum Microtox acute toxicity removal was found in SMM=20 mg/l after 180 min and at 60°C. It was observed an inhibition effect of SMM=40 mg/l to Microtox with *Vibrio fischeri* after 180 min, and at 60°C. 93.27% maximum *Daphnia magna* acute toxicity removal was obtained in SMM=20 mg/l after 180 min and at 60°C, respectively. It was obtained an inhibition effect of SMM=40 mg/l to *Daphnia magna* after 180 min and at 60°C. Increasing the SMM concentrations from 5 to 40 mg/l did not have a positive effect on the decrease of EC_{50} values. SMM concentrations > 20 mg/l decreased the acute toxicity removals by hindering the PDP. Similarly, a significant contribution of increasing SMM concentration to acute toxicity removal at 60°C after 180 min was not observed. Low toxicity removals found at high SMM concentrations could be attributed to their detrimental effect on *Aliivibrio fischeri* and *Daphnia magna.*

As a result, the CuO/ZrO$_2$ NCs during PDP in PI ww was stable in harsh environments such as acidic, alkaline, saline, and then was still effective process. When the amount of contaminant was increased, the a novel CuO/ZrO$_2$ NCs during PDP performance was still considerable. The synthesis and optimization of CuO/ZrO$_2$ heterostructure photocatalyst provides insights into the effects of preparation conditions on the material's characteristics and performance, as well as the application of the effectively designed photocatalyst in the removal of antibiotics, which can potentially be deployed for purifying wastewater, especially PI ww. Finally, the combination of a simple, easy operation preparation process, excellent performance and cost effective, makes this CuO/ZrO$_2$ NCs a promising option during PDP in PI ww treatment.

COMPETING INTERESTS

Authors have declared that no competing interests exist.

REFERENCES

1. Idham MF, Abdullah B, Yusof KM. Effects of two cycle heat treatment on the microstructure and hardness of ductile iron. Pertanika J Sci Technol. 2017;25:99-106.

2. Idham MF, Falyouna O, Eljamal O. Effect of graphene oxide synthesis method on the adsorption performance of pharmaceutical contaminants. Proc Int Exch Innov Conf Eng Sci. 2021;7:232-39.

3. Arenas NE, Melo VM. Producción pecuaria y emergencia de antibiótico resistencia en Colombia: Revisión sistemática. Infectio. 2018;22:110-19.

4. Pellerito A, Ameen SM, Micali M, Caruso G. Antimicrobial substances for food packaging products: the current situation. J AOAC Int. 2018;101(4):942-47.

5. Fridkin S, Baggs J, Fagan R, Magill S, Pollack LA, Malpiedi P. et al. Vital signs: improving antibiotic use among hospitalized patients. MMWR-Morb Mortal Wkly Rep. 2014;63(9):194-200.

6. Tamma PD, Avdic E, Li DX, Dzintars K, Cosgrove SE. Association of adverse events with antibiotic use in hospitalized patients. JAMA Intern Med. 2017;177: 1308-15.

7. Huo TI. The first case of multidrug-resistant NDM−1-harboring Enterobacteriaceae in Taiwan: here comes the superbacteria! J Chin Med Assoc. 2010;73:557-58.

8. Ferri M, Ranucci E, Romagnoli P, Giaccone V. Antimicrobial resistance: A global emerging threat to public health systems. Crit Rev Food Sci. 2017;57:2857-76.

9. Tan L, Li LY, Ashbolt N, Wang XL, Cui YX, Zhu X. et al. Arctic antibiotic resistance gene contamination, a result of anthropogenic activities and natural origin. Sci Total Environ. 2018;621:1176-84.

10. Tong S, Pan J, Lu S, Tang J. Patient compliance with antimicrobial drugs: a Chinese survey. Am J Infect Control. 2018;46:E25-E29.

11. Alygizakis NA, Gago-Ferrero P, Borova VL, Pavlidou A, Hatzianestis I, Thomaidis NS. Occurrence and spatial distribution of 158 pharmaceuticals, drugs of abuse and related metabolites in offshore seawater. Sci Total Environ. 2016;541:1097-05.

12. Casanova LM, Sobsey MD. Antibiotic-resistant enteric bacteria in environmental waters. Water. 2016;8(12):561-67.

13. Zhang L-H, He Y-W, Chen M, Gao M, Qiu T-L, Wang X-M. Pollution characteristics of antibiotic resistant bacteria from atmospheric environment of animal feeding operations. Huan Jing Ke Xue. 2016;37:4531-37.

14. Jiménez-Tototzintle M, Ferreira IJ, da Silva Duque S, Guimarães Barrocas PR, Saggioro EM. Removal of contaminants of emerging concern (CECs) and antibiotic resistant bacteria in urban wastewater using UVA/TiO2/H2O2 photocatalysis. Chemosphere. 2018;210:449-57.

15. Kerrigan JF, Sandberg KD, Engstrom DR, LaPara TM, Arnold WA. Small and large-scale distribution of four classes of antibiotics in sediment: association with metals and antibiotic resistance genes. Environ Sci Process Impacts. 2018;20:1167-79.

16. McConnell MM, Truelstrup Hansen L, Jamieson RC, Neudorf KD, Yost CK, Tong A. Removal of antibiotic resistance genes in two tertiary level municipal wastewater treatment plants. Sci Total Environ. 2018;643:292-300.

17. Karthikeyan KG, Meyer MT. Occurrence of antibiotics in wastewater treatment facilities in Wisconsin, USA., Sci Total Environ. 2006;361:196-207.

18. Dinh QT, Moreau-Guigon E, Labadie P, Alliot F, Teil M-J, Blanchard M. et al. Occurrence of antibiotics in rural catchments. Chemosphere. 2017;168:483-90.

19. Dong D, Zhang L, Liu S, Guo Z, Hua X. Antibiotics in water and sediments from Liao River in Jilin Province, China: occurrence, distribution, and risk assessment. Environ Earth Sci. 2016;75(16):1202, ref.45.

20. Siedlewicz G, Białk-Bielinska A, Borecka M, Winogradow A, Stepnowski P, Pazdro K. Presence, concentrations and risk assessment of selected antibiotic residues

in sediments and near-bottom waters collected from the Polish Coastal Zone in the Southern Baltic Sea-Summary of 3years of studies. Mar Pollut Bull. 2018;129:787-801.

21. Barry S. Dangerously high levels of antibiotics found in world's major rivers, says study. World news global study, Euronews. 2019;1:1-10.

22. Maycock DS, Watts CD. Pharmaceuticals in drinking water. Encycl Environ Heal. 2011;472-84.

23. Fekadu S, Alemayehu E, Dewil R, Van der Bruggen B. Pharmaceuticals in freshwater aquatic environments: a comparison of the african and european challenge. Sci Total Environ. 2019;654:324-37.

24. Wang J, Hao J, Liu D, Qin S, Chen C, Yang C. et al. Flower stamen-like porous boron carbon nitride nanoscrolls for water cleaning. Nanoscale. 2017;9:9787-91.

25. Wang X, Wang A, Lu M, Ma J. Synthesis of magnetically recoverable Fe^0/graphene-TiO_2 nanowires composite for both reduction and photocatalytic oxidation of metronidazole. Chem Eng J. 2017;337:372–84.

26. Wang W, Zhu Q, Dai Q, Wang X. Fe doped CeO_2 nanosheets for catalytic oxidation of 1,2-dichloroethane: effect of preparation method. Chem Eng J. 2017;307:1037-46.

27. Yang X, Chen Z, Zhao W, Liu C, Qian X, Zhang M. et al. Recent advances in photodegradation of antibiotic residues in water. Chem Eng J. 2021;405:126806.

28. Akyon B, McLaughlin M, Hernández F, Blotevogel J, Bibby K. Characterization and biological removal of organic compounds from hydraulic fracturing produced water. Environ Sci Process. 2019;21:279-90.

29. Zhang C, Li Y, Shuai D, Shen Y, Xiong W, Wang L. Graphitic carbon nitride (g-C_3N_4)-based photocatalysts for water disinfection and microbial control: A review. Chemosphere. 2019;214:462-79.

30. de Souza Santos LV, Meireles AM, Lange LC. Degradation of antibiotics norfloxacin by fenton, UV and UV/H_2O_2. J Environ Manag. 2015;154:8-12.

31. Zhong Y, Han L, Yin X, Li H, Fang D, Hong G. Three dimensional functionalized carbon/tin(IV) sulfide biofoam for photocatalytical purification of chromium(VI)-containing wastewater. ACS Sustain Chem Eng. 2018;6:10660-67.

32. Alagha O, Ouerfelli N, Kochkar H, Almessiere MA, Slimani Y, Manikandan A. et al. Kinetic modeling for photo-assisted penicillin G degradation of (Mn0.5Zn0.5)[CdxFe2-x]O4 (x ≤ 0.05) nanospinel ferrites. Nanomaterials. 2021;11:970-86.

33. Yang L, Zhu Y-J, He G, Li H, Tao J-C. multifunctional photocatalytic filter paper based on ultralong nanowires of the calcium-alendronate complex for high-performance water purification. ACS Appl Mater Interfaces. 2022;14:9464-79.

34. Hu L, Flanders PM, Miller PL, Strathmann TJ. Oxidation of sulfamethoxazole and related antimicrobial agents by TiO_2 photocatalysis. Water Res. 2007;41:2612-26.

35. Sukul P, Spiteller M. Sulfonamides in the environment as veterinary drugs. Rev Environ Contam Toxicol. 2006;187:67-101.

36. Thiele-Bruhn S. Pharmaceutical antibiotic compounds in soils-a review. J Plant Nutr Soil Sci. 2003;166:145-67.

37. Sukul P, Lamshoft M, Zühlke S, Spiteller M. Sorption and desorption of sulfadiazine in soil and soil-manure systems. Chemosphere. 2008;73:1344-50.

38. Barber LB, Keefe SH, LeBlanc DR, Bradley PM, Chapelle FH, Meyer MT. et al. Fate of sulfamethoxazole, 4-nonylphenol, and 17b-estradiol in groundwater contaminated by wastewater treatment plant effluent. Environ Sci Technol. 2009;43:4843-50.

39. Ryan CC, Tan DT, Arnold WA. Direct and indirect photolysis of sulfamethoxazole and trimethoprim in wastewater treatment plant effluent. Water Res. 2011;45:1280-86.

40. Le TX, Munekage Y. Residues of selected antibiotics in water and mud from shrimp ponds in mangrove areas in Viet Nam. Mar Pollut Bull. 2004;49:922-29.

41. Dietze JE, Scribner EA, Meyer MT, Kolpin DW. Occurrence of antibiotics in water from 13 fish hatcheries, 2001-2003. Int J Environ An. 2005;85:1141-52.

42. Lin AY-C, Yu T-H, Lin C-F. Pharmaceutical contamination in residential, industrial, and agricultural waste streams: risk to aqueous environments in Taiwan. Chemosphere. 2008;74:131-41.

43. García-Galan MJ, Díaz-Cruz MS, Barcelo D. Determination of 19 sulfonamides in environmental water samples by automated on-line solid-phase extraction-liquid chromatography-tandem mass

spectrometry (SPE-LC-MS/ MS). Talanta. 2010;81:355-66.

44. Luo Y, Xu L, Rysz M, Wang Y, Zhang H, Alvarez PJJ. Occurrence and transport of tetracycline, sulfonamide, quinolone, and macrolide antibiotics in the Haihe River basin, China. Environ Sci Technol. 2011;45:1827-33.

45. Tamtam F, Mercier F, Le Bot B, Eurin J, Tuc Dinh Q, Clement M. et al. Occurrence and fate of antibiotics in the Seine River in various hydrological conditions. Sci Total Environ. 2008;393:84-95.

46. Tamtam F, van Oort F, Le Bot B, Dinh T, Mompelat S, Chevreuil M. et al. Assessing the fate of antibiotic contaminants in metal contaminated soils four years after cessation of long-term waste water irrigation. Sci Total Environ. 2011;09:540-47.

47. Batt AL, Snow DD, Aga DS. Occurrence of sulfonamide antimicrobials in private water wells in Washington County, Idaho, USA. Chemosphere. 2006;64:1963-71.

48. García-Galan MJ, Garrido T, Fraile J, Ginebreda A, Díaz-Cruz MS, Barcelo D. Simultaneous occurrence of nitrates and sulfonamide antibiotics in two ground water bodies of Catalonia (Spain). J Hydrol. 2010;383:93-101.

49. Camacho-Munoz D, Martín J, Santos JL, Aparicio I, Alonso E. Concentration evolution of pharmaceutically active compounds in raw urban and industrial wastewater. Chemosphere. 2014;111:70-79.

50. Kim S, Aga DS. Potential ecological and human health impacts of antibiotics and antibiotic-resistant bacteria from wastewater treatment plants. J Toxicol Environ Health B. 2007;10:559-73.

51. Baran W, Sochacka J, Wardas W. Toxicity and biodegradability of sulfonamides and products of their photocatalytic degradation in aqueous solutions. Chemosphere. 2006;65:1295-99.

52. Littlefield NA, Gaylor DW, Blackwell BN, Allen RR. Chronic toxicity/carcinogenicity studies of sulfamethazine in B6C3F1 mice. Food Chem Toxicol. 1989;27:455–63.

53. Littlefield NA, Sheldon WG, Allen R, Gaylor DW. Chronic toxicity/carcinogenicity studies of sulfamethazine in Fischer 344/N rats: two-generation exposure. Food Chem Toxicol. 1990;28:157–67.

54. Reel JR, Tyl RW, Lawton AD, Lamb JC. Reproductive toxicity of sulfamethazine in Swiss CD-1 mice during continuous breeding. Fundam Appl Toxicol. 1992;18:609–15.

55. Pi Y, Feng J, Sun J, Sun J. Facile, effective, and environmentfriendly degradation of sulfamonomethoxine in aqueous solution with the aid of a UV/Oxone oxidative process. Environ Sci Pollut Res. 2013;20:8621–28.

56. Yan J, Lei M, Zhu L, Anjum MN, Zou J, Tang H. Degradation of sulfamonomethoxine with Fe_3O_4 magnetic nanoparticles as heterogeneous activator of persulfate. J Hazard Mater. 2011;186:1398–1404.

57. Hui SJ, Lan FJ, Hui SS, Qing PIY, Ke SM, Yan S. Degradation of the antibiotic sulfamonomethoxine sodium in aqueous solution by photo-Fenton oxidation. Environ Sci Technol. 2012;57:558–64.

58. Zhu A, Zhu W, Wub Z, Jing Y. Recovery of clindamycin from fermentation wastewater with nanofiltration membranes. Water Res. 2003;37(15):3718-32.

59. Anjali R, Shanthakumar S. Insights on the current status of occurrence and removal of antibiotics in wastewater by advanced oxidation processes. J Environ Manage. 2019;246:51-62.

60. Liu J, Yin ML, Xiao TF, Zhang CS, Tsang DCW, Bao ZA. et al. Thallium isotopic fractionation in industrial process of pyrite smelting and environmental implications. J Hazard Mater. 2020;384(11):121378.

61. Wang J, Zhuan R. Degradation of antibiotics by advanced oxidation processes: An overview. Sci Total Environ. 2020;701:135023.

62. Liu W, Li Z, Kang Q, Wen L. Efficient photocatalytic degradation of doxycycline by coupling α-Bi_2O_3/g-C_3N_4 composite and H_2O_2 under visible light. Environ Res. 2021;197:110925.

63. Liu YP, Lv Y-T, Guan J-F, Khoso FM, Jiang X-Y, Chen J. et al. Rational design of three-dimensional graphene/graphene oxide-based architectures for the efficient adsorption of contaminants from aqueous solutions. J Mol Liq. 2021;343:117709.

64. Homem V, Santos L. Degradation and removal methods of antibiotics from aqueous matrices-A review. J Environ Manage. 2011;92(10):2304-47.

65. Bagheri S, TermehYousefi SA, Do T-O. Photocatalytic pathway toward degradation of environmental pharmaceutical pollutants: Structure, kinetics and

mechanism approach. Catal Sci Technol. 2017;7:4548-69.

66. Cuerda-Correa EM, Alexandre-Franco MF, Fernandez-Gonzalez C. Advanced oxidation processes for the removal of antibiotics from water, an overview. Water. 2020;12(1):102-53.

67. Lima VB, Goulart LA, Rocha RS, Steter JR, Lanza MRV. Degradation of antibiotic ciprofloxacin by different AOP systems using electrochemically generated hydrogen peroxide. Chemosphere. 2020;247:125807.

68. Biancullo F, Moreira NFF, Ribeiro AR, Manaia CM, Faria JL, Nunes OC. et al. Heterogeneous photocatalysis using UVA-LEDs for the removal of antibiotics and antibiotic resistant bacteria from urban wastewater treatment plant effluents. Chem Eng J. 2019;367:304-13.

69. Wei Z, Liu J, Shangguan W. A review on photocatalysis in antibiotic wastewater: Pollutant degradation and hydrogen production. Chinese J Catal. 2020;41(10):1440-50.

70. Ahmed MM, Brienza M, Goetz V, Chiron S. Solar photo-fenton using peroxymonosulfate for organic micropollutants removal from domestic wastewater: Comparison with heterogeneous TiO_2 photocatalysis. Chemosphere. 2014;117:256-61.

71. Wang Y, Sun H, Ang HM, Tade MO, Wang S. Facile synthesis of hierarchically structured magnetic $MnO_2/ZnFe_2O_4$ hybrid materials and their performance in heterogeneous activation of peroxymonosulfate. ACS Appl Mater Interfaces. 2014;6(22):19914-23.

72. Ren Y, Lin L, Ma J, Yang J, Feng J, Fan Z. Sulfate radicals induced from peroxymonosulfate by magnetic ferrospinel MFe_2O_4 (M ¼ Co, Cu, Mn, and Zn) as heterogeneous catalysts in the water. Appl Catal B: Environ. 2015;165:572-78.

73. Mady AH, Baynosa ML, Tuma D, Shim J-J. Heterogeneous activation of peroxymonosulfate by a novel magnetic 3D gamma-MnO_2@$ZnFe_2O_4$/rGO nanohybrid as a robust catalyst for phenol degradation. Appl Catal B: Environ. 2019;244:946-56.

74. Zhu S, Xu Y, Zhu Z, Liu Z, Wang W. Activation of peroxymonosulfate by magnetic Co-Fe/SiO_2 layered catalyst derived from iron sludge for ciprofloxacin degradation. Chem Eng J. 2020;384:123298.

75. Długosz O, Szostak K, Staroń A, Pulit-Prociak J, Banach M. Methods for reducing the toxicity of metal and metal oxide NPs as biomedicine. Materials (Basel). 2020;13(2):279.

76. Sohail MI, Ayub MA, Ziaur Rehman M, Azhar M, Farooqi ZUR, Siddiqui A. et al. Chapter 7-Sufficiency and toxicity limits of metallic oxide nanoparticles in the biosphere. In: Tahir MB, Sagir M, Asiri AM, editors. Nanomaterials: Synthesis, Characterization, Hazards and Safety: Elsevier; 2021:145-221.

77. Sahu K, Singhal R, Mohapatra S. Morphology Controlled CuO Nanostructures for efficient catalytic reduction of 4-nitrophenol. Catal Letters. 2019;150(2):471-81.

78. Karuppannan SK, Ramalingam R, Mohamed Khalith SB, Musthafa SA, Dowlath MJH, Munuswamy-Ramanujam G. et al. Copper oxide nanoparticles infused electrospun polycaprolactone/gelatin scaffold as an antibacterial wound dressing. Mater Lett. 2021;294:129787.

79. Majumdar D, Ghosh S. Recent advancements of copper oxide based nanomaterials for supercapacitor applications. J Energy Storage. 2021;34:101995.

80. Aslani A. Controlling the morphology and size of CuO nanostructures with synthesis by solvo/hydrothermal method without any additives. Physica B: Condensed Matter. 2011;406(2):150-54.

81. Jung A, Cho S, Cho WJ, Lee K-H. Morphology-controlled synthesis of CuO nano- and microparticles using microwave irradiation. Korean J Chem Eng. 2011;29(2):243-48.

82. Dhineshbabu NR, Rajendran V, Nithyavathy N, Vetumperumal R. Study of structural and optical properties of cupric oxide nanoparticles. Applied Nanoscience. 2015;6(6):933-39.

83. Boltaev GS, Ganeev RA, Krishnendu PS, Zhang K, Guo C. Nonlinear optical characterization of copper oxide nanoellipsoids. Sci Rep. 2019;9(1):11414.

84. Alhazime AA. Effect of nano CuO doping on structural, thermal and optical properties of PVA/PEG blend. J Inorg Organomet Polym Mater. 2020;30(11): 4459-67.

24

85. Iqbal M, Thebo AA, Shah AH, Iqbal A, Thebo KH, Phulpoto SN. et al. Influence of Mn-doping on the photocatalytic and solar cell efficiency of CuO nanowires. Inorg Chem Commun. 2017;76:71-76.

86. Gerawork M. Photodegradation of methyl orange dye by using zinc oxide–copper oxide nanocomposite. Optik.. 2020;216: 164864.

87. Raizada P, Sudhaik A, Patial S, Hasija V, Parwaz Khan AA, Singh P. et al. Engineering nanostructures of CuO-based photocatalysts for water treatment: Current progress and future challenges. Arab J Chem. 2020;13(11):8424-57.

88. Aadil M, Rahman A, Zulfiqar S, Alsafari IA, Shahid M, Shakir I. et al. Facile synthesis of binary metal substituted copper oxide as a solar light driven photocatalyst and antibacterial substitute. Adv Powder Technol. 2021;32(3):940-50.

89. Abul Kareem Alghurabi MN, Shakir Mahmood R, Salim ET, Hamza Alhasan SF, Khalid FG. Structure, optical, and morphological investigations of nano copper oxide prepared using RPLD at different laser wavelength effects. Materials Today: Proceedings. 2021; 42:2497-2501.

90. Rachna, Rani M, Shanker U. Synergistic effects of zinc oxide coupled copper hexacyanoferrate nanocomposite: Robust visible-light driven dye degradation. J Colloid Interface Sci. 2021;584:67-79.

91. Pirzada BM, Mir NA, Qutub N, Mehraj O, Sabir S, Muneer M. Synthesis, characterization and optimization of photocatalytic activity of TiO_2/ZrO_2 nanocomposite heterostructures. Mater Sci Eng B. 2015;193:137–45.

92. Aldeen ES, Jalil AA, Mim RS, Alhebshi A, Hassan NS, Saravanan R. Altered zirconium dioxide based photocatalyst for enhancement of organic pollutants degradation: A review. Chemosphere. 2022;304:135349.

93. Ahmed W, Iqbal J. Co doped ZrO_2 nanoparticles: An efficient visible light triggered photocatalyst with enhanced structural, optical and dielectric characteristics. Ceram Int. 2020;46:25833-44.

94. Zhang K, Zhou M, Yu C, Yang K, Li X, Dai W. et al. Construction of S-scheme g-C_3N_4/ZrO_2 heterostructures for enhancing photocatalytic disposals of pollutants and electrocatalytic hydrogen evolution. Dyes Pigm. 2020;180:108525.

95. García-López E, Marcì G, Pomilla F, Paganini M, Gionco C, Giamello E. et al. ZrO_2 Based materials as photocatalysts for 2-propanol oxidation by using UV and solar light irradiation and tests for CO_2 reduction. Catal Today. 2018;313:100–105.

96. Guerrero-Araque D, Acevedo-Peña P, Ramírez-Ortega D, Calderon HA, Gómez R. Charge transfer processes involved in photocatalytic hydrogen production over $CuO/ZrO_2–TiO_2$ materials. Int J Hydrog Energy. 2017;42(15):9744-53.

97. Guerrero-Areque D, Gomez R, Calderon HA. TEM characterization of heterojunctions for photocatalytic application: ZrO_2-TiO_2 and CuO/ZrO_2-TiO_2. Microsc Microanal. 2017;23(S1):2036-37.

98. Renuka L, Anantharaju KS, Vidya YS, Nagaswarupa HP, Prashantha SC, Sharma SC. et al. A simple combustion method for the synthesis of multi-functional ZrO_2/CuO nanocomposites: Excellent performance as Sunlight photocatalysts and enhanced latent fingerprint detection. Appl Catal B: Environ. 2017;210:97-115.

99. Nanda B, Pradhan AC, Parida KM. Fabrication of mesoporous CuO/ZrO_2-MCM-41 nanocomposites for photocatalytic reduction of Cr(VI). Chem Eng J. 2017;316:1122-35.

100. Babu MH, Podder J, Dev BC, Sharmin M. p to n-type transition with wide blue shift optical band gap of spray synthesized Cd doped CuO thin films for optoelectronic device applications. Surf Interfaces. 2020;19:100459.

101. Kumar P, Chandra Mathpal M, Prakash J, Viljoen BC, Roos WD, Swart HC. Band gap tailoring of cauliflower-shaped CuO nanostructures by Zn doping for antibacterial applications. J Alloys Compd. 2020;832:154968.

102. Lipps WC, Braun-Howland EB, Baxter TE. Standard methods for the examination of water and wastewater. In Lipps WC, Braun-Howland EB, Baxter TE, editors. American Public Health Association (APHA), American Water Works Association (AWWA), Water Environment Federation (WEF), Elevate Your Standards. 24th ed. (American Public Health Association 800 I Street, NW Washington DC: 20001-3770, USA. December 1, 2022; ISBN:9780875532998, 2022.

103. Olthof M, Eckenfelder WW. Coagulation of textile wastewater. Text Chem Color. 1976;8:18-22.

104. Eckenfelder WW. Industrial water pollution control (2nd ed), Signapore: McGraw-Hill Inc.;1989.

105. Lange B. LUMISmini, Operating Manual. Dusseldorf, Germany: Dr Bruno LANGE., 1994.

106. Lange B. Vibrio fischeri -Microtox LCK 491 kit. Germany: Dr LANGE; 2010.

107. Lange B. LUMIXmini type luminometer. Dusseldorf: Dr LANGE Company., 1996.

108. Zar JH. Biostatistical analysis, Prentice-Hall, Englewood Cliffs; 1984.

109. Statgraphics Centurion XV, sofware, StatPoint Inc, Statgraphics Centurion XV, Herndon, VA, USA; 2005.

110. Eddy DR, Puri FN, Noviyanti AR. Synthesis and photocatalytic activity of silica-based sand quartz as the supporting TiO_2 photocatalyst. Proced Chem. 2015; 17:55-58.

Peer-review history:
The peer review history for this paper can be accessed here:
https://www.sdiarticle5.com/review-history/99466